Superparamagnetic Iron Oxide and Ferrite Nanoparticles for MRI

Thomas Vangijzegem[1], Levy Van Leuven[1], Dimitri Stanicki[1], Robert N. Muller[1,2], Sophie Laurent[1.2]

[1] General, Organic and Biomedical Chemistry Unit, NMR and Molecular Imaging Laboratory, University of Mons, B-7000 Mons, Belgium

[2] Center for Microscopy and Molecular Imaging, Rue Adrienne Bolland, 8, B-6041 Gosselies, Belgium

Thomas.vangijzegem@umons.ac.be, Levy.VANLEUVEN@umons.ac.be, Dimitri.stanicki@umons.ac.be; Robert.Muller@umons.ac.be, Sophie.laurent@umons.ac.be

Table of contents

Abstract

Starting from the mid-1990s, colloidal suspensions of superparamagnetic nanoparticles, consisting of iron oxides, magnetite (Fe_3O_4), maghemite (Fe_2O_3) or other ferrites, were introduced as contrast agents for magnetic resonance imaging (MRI) due to their very large magnetic moments and their suitable biocompatibility for *in vitro* and *in vivo* applications. Within the MRI field, superparamagnetic iron oxide nanoparticles (SPION) are well known as T_2 contrast agents, producing significant signal loss on T_2- and T_2*-weighted images. Several SPION formulations have been designed and clinically evaluated as MRI contrast agents, initially as liver-specific contrast agents due to their fast clearance by the mononuclear phagocyte system, but also for other MRI applications such as blood-pool imaging, lymph node imaging or gastrointestinal imaging. In this chapter, we discuss the fundamental aspects of iron oxide nanoparticles with regard to their use as contrast agents for magnetic resonance imaging (MRI). Specifically, the first section of this chapter describes the theoretical basis of proton relaxation induced by the presence of SPION and provides a detailed description of the superparamagnetic relaxation theory to understand the performances of SPION as contrast agents for MRI. The second part of this chapter focuses on clinically developed SPION-based contrast agents, with a particular emphasis on T_2 contrast agents and reasons for their withdrawal from clinical settings. We then discuss recent applications of SPION as efficient T_1 contrast agents, including the stringent physicochemical requirements which have to be fulfilled for their satisfactory use as clinically-preferred T_1 contrast agents when gadolinium-based contrast agents (GBCA) are contraindicated for patients at risk with renal impairment.

Keywords

Magnetic resonance imaging (MRI) ; Superparamagnetic iron oxide nanoparticles (SPION) ; Ferrite nanoparticles ; Contrast agents ; Longitudinal relaxation ; Transverse relaxation

1. Introduction

Iron is the most abundant transition metal in the Earth's crust and, due to its high reactivity, reacts with water and oxygen to yield iron oxides (iron oxides, iron hydroxides and iron oxyhydroxides)[1]. Up to now, 16 phases of oxides, hydroxides and oxyhydroxides have been identified and classified according to their compositions and molecular structures[2]. Among the iron oxides subgroup, hematite (α-Fe_2O_3), magnetite (Fe_3O_4) and maghemite (γ-Fe_2O_3) are the most naturally occurring iron oxide minerals, accompanied by wüstite (FeO). The properties of these three abundant iron oxides are listed in Table 1[3].

Magnetite and maghemite are the only two iron oxides exhibiting strong magnetic properties *i.e.* high values of saturation magnetization (M_S). At the macroscale, both phases exhibit ferrimagnetic ordering characterized by the formation of organized sub-networks with uncompensated magnetic moments. Such arrangement leads to the formation of a multidomain structure showing magnetic hysteresis (Figure 1A; Reprinted from [4]). This important characteristic leads to the presence of remanent magnetization (M_R) and coercivity (H_C) in the (de)magnetization curves of ferrimagnetic compounds (Figure 1A; Orange curve). However, when their size decreases to the nanoscale level, transition occurs from nanomaterials bearing a multidomain structure towards single-domain nanoparticles exhibiting a peculiar magnetic behavior called superparamagnetism. The absence of domains leads to the formation of uniformly magnetized nanoparticles without remanence or coercivity (Figure 1A; Green curve). This transition towards single-domain nanoparticles exhibiting superparamagnetism usually occurs when decreasing their size below 25 nm (Superparamagnetic size (r_{SP}); Figure 1B).

This unique form of magnetism has made iron oxide nanoparticles remarkable nanoscale candidates for numerous applications in the biomedical field as they exhibit a rapid "on-off" switching capability, *i.e.* they reveal their magnetic properties only when subjected to an external magnetic field and retain no residual magnetism once the applied magnetic field is

removed. Superparamagnetic iron oxide nanoparticles (SPION) behave similarly to paramagnets, except that the magnetic susceptibility of one particle is several orders of magnitude higher than the one of paramagnetic substances, hence resulting in higher magnetic properties[5]. Moreover, the return to an equilibrium non-magnetized state after removal of the magnetic field makes SPION unlikely to agglomerate when they are introduced into living systems, thus increasing their half-life circulation times and avoiding the threat of cardiovascular disorders such as thrombosis or blockage of blood capillaries due to particle agglomeration[6,7].

As a result of their superparamagnetic state, combined with their excellent toxicological and safety profiles[8], SPION have been used as probes for diagnosis and/or as therapeutic substances in various applications of the biomedical field such as magnetic resonance imaging, targeted drug delivery[9–13], cell labeling[14–17], magnetic fluid hyperthermia[18,19], gene therapy[20,21], tissue engineering[22,23], and more recently magnetic particle imaging[24] and radiation therapy[25–27]. SPION have been an integral part in the development of MRI due their ability to shorten the relaxation rates of surrounding water molecules and improve the contrast. This ability originates from local magnetic field inhomogeneities induced by SPION when submitted to an external magnetic field. Theoretical relaxation models have been developed to describe the influence of SPION on proton relaxation rates[28,29].

2. Superparamagnetic relaxation theory

Single-domain nanoparticles are characterized by magnetic anisotropy, *i.e.* the magnetic moments of SPION are aligned in energetically favourable positions called “easy axis” or “anisotropy axis”. Considering spherical nanoparticles, anisotropy is often considered to be uniaxial, that is, with magnetic moments aligned either parallel or anti-parallel to a single anisotropy axis (Figure 2).

The anisotropy energy (E_A), defined as the energy required to flip from one easy axis to another, is proportional the volume of the considered crystal according to equation 1:

$$E_A = K_A.V.sin^2\theta \qquad (1)$$

Where V is the volume of the crystal, θ is the angle between the magnetic moment vector and the easy axis and K_A is an anisotropy constant depending on the physicochemical properties of the considered material.

The volume dependence of anisotropy energy involves that, when decreasing the nanoparticle size, the anisotropy energy decreases until being inferior to thermal agitation energy (kT). In this situation, thermal fluctuations are sufficient to induce flips of the magnetic moments between the different anisotropy axes. This flipping phenomenon was initially described by Néel who described the time between two flips between the easy axes, known as the Néel relaxation time (τ_N), given as (Equation 2):

$$\tau_N = \tau_0 e^{\frac{E_A}{kT}} \quad (2)$$

Where τ_0 is the pre-exponential factor, k is the Boltzmann constant ($1{,}380649.10^{-23}$ $m^2.kg.s^{-2}.K^{-1}$), T is the sample temperature (K) and E_A is the anisotropy energy.

Besides Néel relaxation, SPION dispersed in a liquid medium are also subject to Brownian relaxation, corresponding to the complete rotation of SPION due to collisions with solvent molecules. The resulting Brownian relaxation time (τ_B) is given as (Equation 3):

$$\tau_B = \frac{3V\eta}{kT} \qquad (3)$$

Where V is the particle volume and η is the fluid viscosity.

The global relaxation rate of SPION dispersed in a liquid medium is dependent upon the two mechanisms of relaxation and it can be expressed as the sum of the two contributions according to equation 4.

$$\frac{1}{\tau} = \frac{1}{\tau_N} + \frac{1}{\tau_B} \quad (4)$$

Depending on the size of the considered crystal, one of the two relaxation mechanisms will dominate the relaxation of the system. Néel relaxation time will be dominant for small nanoparticles (characterized by lower anisotropy energy) while larger particles will mainly relax through the Brownian contribution of relaxation.

This global relaxation mechanism is only related to the relaxation of the nanoparticle's magnetic moment, and not directly the relaxation of water protons. However, dipolar coupling between the magnetic moment of SPION and the magnetic moments of water protons is greatly responsible for the modification of relaxation rates. Water protons in the presence of superparamagnetic nanoparticles experience magnetic fluctuations due to their free diffusion through magnetic inhomogeneities produced by the dipolar magnetic field (Figure 3). This interaction is modulated by water diffusion, but also by Néel and Brownian relaxation rates of the superparamagnetic nanoparticles[30].

2.1. Longitudinal relaxation

The description of the superparamagnetic relaxation phenomena is based on theoretical model established by A. Roch, R. Muller and P. Gillis (theoretical model known as the RMG model or Superparamagnetic (SPM) model[28]). This model is built upon the original relaxation theory described for paramagnetic compounds. However, in the case of SPION, the model has been adapted to consider their much higher magnetic moment and their anisotropy. Inner-sphere relaxation does not contribute significantly to the proton relaxation which is rather defined by an outer-sphere mechanism where the dipolar interaction is modulated by both Néel relaxation and water diffusion, the latter being defined by the translational diffusion time (τ_D = r²/D where r is the crystal radius and D the water diffusion coefficient).

The RMG model enables understanding of the proton longitudinal relaxation rate in aqueous suspensions of SPION. This theoretical approach assumes a uniform distribution of crystals with uniaxial anisotropy within pure water and is valid for the estimation of proton longitudinal relaxation rate in the presence of both large and small crystals (*i.e.* particle radius above and below 7.5 nm, respectively) respecting the Redfield condition[28,29]. Therefore, distinction should be made according to the size of the considered SPION and the relative strength of the external magnetic field.

Large crystals (particle radius > 7.5 nm) are characterized by high anisotropy energy inducing the locking of the magnetic moment onto the anisotropy axis.

At low magnetic field, flips of the magnetic moment between the different easy axes can occur, the dipolar interaction is therefore modulated by the Néel relaxation time and the translational diffusion time τ_D. In this case, longitudinal relaxation rate is given by equation 5, Néel relaxation and water diffusion are introduced thanks to the Freed spectral density[31] (J_F; Equation 6):

$$R_1 = \frac{1}{T_1} = \frac{32\pi}{405}\gamma^2\mu^2\left(\frac{N_A C}{r^3}\right)[10J_F(\omega_I, \tau_D, \tau_N)] \qquad (5)$$

$$\text{With } J_F(\omega_I, \tau_D, \tau_N) = R_e\left[\frac{1+\frac{1}{4}\Omega^{\frac{1}{2}}}{1+\Omega^{\frac{1}{2}}+\frac{4}{9}\Omega+\frac{1}{9}\Omega^{\frac{3}{2}}}\right] \text{ and } \Omega = i\omega_I\tau_D + \frac{\tau_D}{\tau_N} \qquad (6)$$

Where γ is the proton gyromagnetic ratio, μ is the electron magnetic moment, N_A is the Avogadro number, C is the molar concentration of superparamagnetic compound, r is the crystal radius, ω_I is the proton angular frequency, τ_D is the translational correlation time of water molecules (equal to the square of crystal radius (r) divided by the diffusion constant (D)).

Néel relaxation cannot occur at high magnetic field, magnetic moments remain locked onto the easy axis and Néel relaxation time is much longer. Relaxation is therefore only influenced by

diffusion of water protons. In this case, Ayant spectral density[32] (J_A) can be used to describe the relaxation (Equation 7 and J_A; Equation 8):

$$R_1 = \frac{1}{T_1} = \frac{32\pi}{405}\gamma^2\mu^2\left(\frac{N_A C}{r^3}\right)\left[9L^2(\alpha)J_A\left(\sqrt{2\omega_I\tau_D}\right)\right] \qquad (7)$$

$$\text{With } J_A = \frac{1+\frac{5\mu}{8}+\frac{\mu^2}{8}}{1+\mu+\frac{\mu^2}{2}+\frac{\mu^3}{6}+\frac{4\mu^4}{81}+\frac{\mu^5}{81}+\frac{\mu^6}{648}} \qquad (8)$$

At intermediate magnetic field, both contributions influence the global relaxation mechanism. The weighting given to each contributions is expressed using a linear combination of equations 5 and 7. The Langevin function (L(α)), which gives the average magnetization of the sample, is used to mathematically describe the combination of the low magnetic field and high magnetic field contributions (equation 9).

$$R_1 = \frac{1}{T_1} = \frac{32\pi}{405}\gamma^2\mu^2\left(\frac{N_A C}{r^3}\right)\left\{\begin{array}{c}\left(\frac{L(\alpha)}{\alpha}\right)21J_F(\omega_I,\tau_D,\tau_N) \\ +9\left[1-L^2(\alpha)-2\left(\frac{L(\alpha)}{\alpha}\right)\right]J_F(\omega_I,\tau_D,\tau_N)+9L^2(\alpha)J_A\left(\sqrt{2\omega_I\tau_D}\right)\end{array}\right\} \qquad (9)$$

Using these field-dependent contributions, the RMG model enables the fitting of the relaxation curves for large nanoparticles. The field dependent (NMRD profile) global relaxation rate resulting from each contribution is depicted in Figure 4 (Reproduced from [33]).

For **small crystals** (particle radius < 7.5 nm), slight adaptation to the RMG model has been made to consider the smaller anisotropy energy of these materials. Smaller anisotropy energy results in attenuated locking of the magnetic moments onto the anisotropy directions[34]. This low anisotropy results in a low field dispersion in the field-dependent curve of small iron oxide nanoparticles. Adaptation of the theoretical model by considering the anisotropy as an empirical parameter (P; Equation 10) allowed a good agreement with experimentally observed NMRD curves.

$$R_1 = \frac{1}{T_1} = \frac{32\pi}{405}\gamma^2\mu^2\left(\frac{N_A C}{r^3}\right)\left\{\begin{array}{c}\left(\frac{L(\alpha)}{\alpha}\right)21PJ_F(\omega_I,\tau_D,\tau_N) + 21(1-P)J_F(\omega_I,\tau_D,\tau_N) + \\ 9\left[1 - L^2(\alpha) - 2\left(\frac{L(\alpha)}{\alpha}\right)\right]J_F(\omega_I,\tau_D,\tau_N) + 9L^2(\alpha)J_A\left(\sqrt{2\omega_I\tau_D}\right)\end{array}\right\} \quad (10)$$

A typical NMRD curve of crystals with low anisotropy energy is depicted in Figure 5. Fitting of the experimental curves with the theoretical model provides information concerning the physicochemical properties of SPION. The curve depicted in Figure 5 can be split in four zones, each of which being associated with a physicochemical parameter of SPION: namely, their Néel relaxation time τ_N, their anisotropy energy E_A, their average radius r_{NMRD}, and their saturation magnetization (M_{SAT}).

Fitting of experimental data using the RMG model is suitable for estimating the physicochemical parameters involved in the relaxation induced by superparamagnetic nanoparticles[35]. These parameters are listed below:

① An estimation of the Néel relaxation time (τ_N) can be obtained from the relaxivity plateau at low field. However, this value remains approximative and is usually used as qualitative information in addition to the other parameters (crystal size and saturation magnetization).

② The low-field dispersion observed for small crystals is an indication of their low anisotropy energy (E_A).

③ The maximum value of longitudinal relaxivity reached at high field reflects the saturation magnetization (M_{SAT}) through the approximation $R_{MAX} \approx C.M_{SAT}^2.\tau_D$ where C is a constant and R_{MAX} is the maximum relaxivity.

④ At high magnetic field, an estimation of the nanoparticle radius (r_{NMRD}) can be obtained from the inflexion point of the NMRD curve. This point, corresponding to the condition $\omega_I.\tau_D \approx 1$, enables the determination of τ_D which subsequently allows the estimation of the

nanoparticle radius (through $\tau_D = r_{NMRD}^2/D$). The estimated value of particle size corresponds to the distance of closest approach of solvent molecules from the center of the particle, perfectly permeable coating is therefore required to correctly estimate the particle size.

NMRD profiles, along with the RMG model enabling the theoretical fitting and the extraction of physical parameters of SPION, are powerful characterization tools to evaluate the efficacy of SPION as contrast agents for MRI. However, one must stress that the parameters extracted from the fitting are averaged values of the effective characteristics of ferrofluids. Moreover, NMRD profiles also offer significant information concerning the colloidal stability of nanoparticle suspensions, as the clustering of superparamagnetic nanoparticles highly influences their relaxometric properties.

2.2. Transverse relaxation

The NMR dispersion of proton transverse relaxivity follows the same trend as longitudinal relaxivity at low field. However, its evolution with increasing magnetic field is different, with transverse relaxivity increasing toward reaching a residual value at high magnetic field, whereas longitudinal relaxivity always decreases toward zero (Figure 6). The residual value of transverse relaxivity is often referred as the "secular contribution" or "secular term"[28]. This contribution arises from local magnetic fields (magnetic inhomogeneities), caused by the magnetic nanoparticles, inducing a loss of coherence of the z-component of the magnetic field. The secular contribution therefore reflects the contribution of local fields causing spins to precess at different frequencies, and therefore affecting the transverse relaxation rate[36].

Particle clustering highly affects the relaxation properties of iron oxide nanoparticles and their efficacy as contrast agents. *In vivo* formation of clusters or aggregates of nanoparticles results in unequal variations of both longitudinal and transverse relaxation rates. Longitudinal relaxivity tends to decrease throughout the clustering process[37] (Figure 7A). However, the transverse relaxation rate follows a bell curve in which it reaches a maximum (at approximately

20 nm) and then decreases (Figure 7B; Reprinted from [38]). The secular term is primarily responsible for the evolution of transverse relaxation. The initial increase of R_2 with agglomeration is provoked by the increase of cluster radius, while further increase of the clusters size leads to protons being almost motionless in the sample, resulting in a decrease of R_2 with aggregation[38].

Aggregated SPION can be regarded as single particles characterized by their own sizes and magnetic moments[38,39]. The marked effect of clustering on both relaxation rates gives rise to magnetic assemblies characterized by very high r_2 values and r_2/r_1 ratios that can reach up to several hundred depending on the strength of the external magnetic field. Some of such SPION-based contrast agents have been clinically approved for T_2-*w* MRI, these agents and their applications are discussed in the next sections.

3. SPION-based contrast agents

Contrast agents based on superparamagnetic nanoparticles are made up of specific iron oxide cores and coating polymeric materials, either natural (such as dextran, carbodydextran, starch, chitosan, etc.) or synthetic (polymers based on polyvinylpyrrolidone (PVP), polyethylene glycol (PEG) polyvinyl alcohol (PVA), etc.)[40]. Inorganic materials such as for example, gold, silver or silica have also been reported as stabilizers for SPION[41]. These hydrophilic coatings are designed to provide nanoparticles with enhanced stability in physiological media and immunological stealthiness.

3.1. SPION-based contrast agents

Due to their very high r_2 values, iron oxide nanoparticles were initially designed for applications as T_2 contrast agents. Several formulations of SPION-based T_2 contrast agents have been developed by pharmaceutical companies and/or are in clinical trials, some of them have also been approved by regulatory bodies for clinical use[42].

Table 2 summarizes clinically developed SPION-based contrast agents and their utility as MRI contrast agents.

3.1.1. Hepatic MRI

Ferumoxides and Ferucarbotran are two liver-specific contrast agents which have been developed for the detection of focal liver lesions. Accumulation of the contrast agents in the normal liver parenchyma surrounding focal liver lesions increases the contrast/noise ratio (CNR) of these lesions, which appear more hyperintense on T_2-weighted images compared to the pre-contrast image[43].

Ferumoxide (Endorem® in Europe (Guerbet); Feridex® in the U.S (Berlex Laboratories); AMI-25) was the first clinically approved SPION-based contrast agent. Particles of ferumoxides are composed of several iron oxide cores (core diameter: 5 nm) embedded in low molecular weight dextran coating. The size of the particles is generally between 120 and 180 nm. Ferumoxides are administered as drip infusions over 30 minutes to avoid potential side effects. Nanoparticles are rapidly taken up by the mononuclear phagocyte system (MPS) and phagocytosed by Kupfer cells (macrophages). Uptake by the liver (80 %) and the spleen (6 - 10 %) occurs quickly and persists for several hours, allowing a broad window for effective MR imaging[44]. The accumulation of ferumoxides into liver tissues allows visualization of liver lesions or tumors due to the absence of Kupfer cells in these abnormal tissues. These products were initially designed for the detection of liver metastases or hepatocellular carcinomas (HCCs)[45,46]. Ferumoxides were withdrawn from the market due to lack of use by radiologists.

Ferucarbotran (Resovist® (Schering AG); SHU 555A) is another liver-specific contrast agent enabling the detection of small focal liver lesions. Resovist consists in 4.2 nm SPION embedded in a carboxydextran coating, with an overall hydrodynamic diameter of 62 nm[47]. Resovist® has a better safety profile compared to ferumoxides, enabling its intravenous injection by bolus.

Resovist® was also assessed for dynamic MRI of the brain, but didn't outreach the diagnosis efficacy of gadopentetate dimeglumine[48].

3.1.2. Lymph node imaging

Ferumoxtran-10 (Sinerem® in Europe (Guerbet); Combidex® in the U.S. (AMAG Pharmaceuticals); AMI-227) is a formulation containing smaller particles (5 nm SPION with low molecular weight dextran coating; hydrodynamic diameter of approximately 30 nm)[49]. Due to their small size, nanoparticles slowly leak into the intravascular space (Figure 8; [50]) from which they are subsequently taken up by macrophages and transported to lymph nodes by way of lymphatic vessels[51]. These were primarily designed for metastatic lymph node imaging due to their prolonged blood half-life. Visualisation of lymph nodes was studied for staging pelvic cancers in a total of 271 patients. However, unconcordant results between three different blinded specialist readers led to abandoning the ferumoxtran-10 clinical development[52]. In 2013, the Radboud University Medical Center (Radboudumc) restarted the production of ferumoxtran-10 for clinical trials on patients with prostate cancer, and succeeded in the detection of metastatic lymph nodes with size down to 2 mm[53]. Ferumoxtran-10 is now available under the brand name Ferrotran® (SPL Medical B.V., Nijmegen, The Netherlands).

3.1.3. Blood-pool imaging

Feruglose (Clariscan®; GE Healthcare; NC100150) and **Ferropharm** (VSOP C184) are SPION-based contrast agents which were designed for blood-pool MRI. Both are composed of single crystals, Feruglose consists of crystals (4 to 7 nm SPION) with a carbohydrate polyethylene glycol (PEG)[54] coating while Ferropharm is made of 4 nm SPIONs with a citrate layer[55]. Feruglose and Ferropharm have small hydrodynamic particle size of 12 and 7 nm, respectively[54,56], enabling them to be used for both T_1-*w* and T_2-*w* imaging. Both agents were shown to be well suited for first-pass magnetic resonance angiography (MRA) experiments[56,57] as well as for perfusion-weighted diagnosis of various organs[58,59].

However, although VSOP C184 and NC100150 have been tested in human clinical trials up to phase II[60–63], none of the formulations received regulatory approval[64].

Ferumoxytol (Feraheme®; AMAG Pharmaceuticals), initially designed and developed as an MRI contrast agent, is now used to treat iron deficiency anemia in adults with chronic kidney disease (CKD)[65,66]. Ferumoxytol is made up of 6.4 nm SPION surrounded by a carbohydrate shell (polyglucose sorbitol carboxymethyl ether). The colloidal particle size is approximately 30 nm[67]. Since its approval as a therapeutic iron supplement by the United State Food and Drug Administration (FDA), Ferumoxytol has seen renewed interest as a contrast agent with great potential for numerous applications in MRI where the use of Gadolinium-based contrast agents is contraindicated[68]. Ferumoxytol has favorable physicochemical characteristics enabling satisfactory contrast-enhanced MRI in different organs at various phases (Figure 9; [69]).

Following i.v. administration, imaging can be performed during the dynamic phase (directly after bolus injection) to provide valuable insight of the blood supply of the brain. During the blood pool phase, Ferumoxytol allows high-resolution contrast-enhanced imaging of the intravascular space (arterial and venous systems, hence enabling the diagnosis of vascular diseases[70,71]. Finally, the disrupted blood-brain barrier of brain lesions allows the progressive leakage of nanoparticles resulting in signal changes occurring in the delayed phase around 24 hours after injection[72]. For example, visualization of malignant brain tumors was demonstrated through delayed enhancement peaking at 24 to 28 hours after administration of Ferumoxytol nanoparticles[73].

3.1.4. Gastrointestinal imaging

Ferumoxsil (Lumirem®; Guerbet; AMI-121) and **Ferristene** (Abdoscan®; Amersham Health; OMP) are SPION-based oral formulations designed for gastrointestinal MRI. Ferumoxsil contains silica-coated particles containing multiple 10 nm SPION, the hydrodynamic diameter

is approximately 300 nm while Ferristene consists of micrometric particles (total particle size is 3.5 µm) coated with polystyrene and filled with SPION having diameters below 50 nm. Ferumoxsil and Ferristene were tested in clinical trials for the darkening of bowel loops but both agents were taken off the market due to lack of users[74].

3.1.5. T_2-weighted MRI with SPION

Other than the clinically developed contrast agents, several other SPION-based compounds with various architectures have been studied for T_2-weighted MRI applications. SPION with larger sizes have higher r_2 values, non-spherical particles such as cubes, octapods or plates have been widely studied and showed enhanced r_1 and r_2 relaxivities[75]. Assembly of nanoparticles into magnetic nanostructures such as amphiphilic polymers, matrices of meso-porous silica or liposomes have also been studied and has proven to be effective for attaining high relaxivity values[76,77].

However, despite the increasing amount of SPION-based nanosystems exhibiting remarkable efficacy as T_2 contrast agents, their transition to clinical trials has been very limited due to their inherent contrast mechanism, producing a signal decreasing effect. Many diseases (bleeding, calcification, metal deposits) naturally induce hypointense areas which can be confused with the presence of T_2 contrast agents. Moreover, SPION generate magnetic inhomogeneities causing distortion of the magnetic field in their close vicinity. This effect, often referred as "blooming effect" or "blooming artifact", causes signal destruction and makes the diagnosis difficult when it comes to determining the exact state of a lesion[78,79], often resulting in an overestimation of the lesion size as depicted in Figure 10.

3.2. SPION as T_1 contrast agents

The major advantage of iron oxide nanoparticles is their biocompatibility which makes them very attractive for biomedical applications. This favourable feature, combined with the ongoing concerns about the toxicity of gadolinium-based contrast agents (GBCA), whether in the case

of patients at risk with nephrogenic systemic fibrosis[80–83] or more recently with findings of long-term retention of Gd in the brain of patients administered with GBCA[84–88], led researchers into developing SPION as T_1 contrast agents for MRI. To that end, several physicochemical prerequisites must be satisfied in order to reach optimal imaging efficacy, those features are described in the next section.

3.2.1. Parameters affecting T_1 contrast with SPION

Using iron oxide nanoparticles with low dimensions (size below 5 nm) that are capable of generating bright contrast on T_1-weighted images is a promising alternative[89]. The r_2/r_1 ratio can be used as an indicator of the suitability of a compound for T_1-*w* or T_2-*w* MRI (Figure 11; Reprinted from [76]). As a rule of thumb, SPION with smaller core *i.e.* smaller r_2/r_1 ratios (< 5) can be used as T_1 contrast agents while bigger nanoparticles are used as T_2 contrast agents ($r_2/r_1 > 10$ at standard clinical field *i.e.* 1.5 T)[90,91].

The link between reduction of r_2/r_1 ratio with the size of nanoparticles can be understood by the spin-canting effect. Magnetic moments of atoms constituting a nanoparticle have different configurations depending on whether they are located on the outer surface of the nanoparticles or inside the nanoparticles. Spins on the outside layer of the nanoparticle have random orientations due to structural disorder at the nanoparticle surface. As these spins are not aligned with the bulk spins of the nanoparticle, they form a magnetically dead layer on the nanoparticle's surface. The spin-canting effect is a finite-size effect, experimental data highlighted that the thickness of the magnetically dead layer is comprised between 0.5 and 0.9 nm depending on the type of nanoparticle[92,93]. Considering a magnetic core of 5 nm, roughly half of the nanoparticle contains randomly oriented spins constituting the magnetically dead region (Figure 12; [94]), assuming a 0.5 nm spin-canted layer[95]. Atoms inside the nanoparticles can also be subjected to spin-canting effects due to cation vacancies in the internal

structure of the magnetic region. Such breakage of the crystal's internal structure disrupt their crystallinity and is also partially responsible for the reduced magnetization of small SPION[96].

Another essential prerequisite is to preserve the stability of SPION *in vivo*, as aggregation would lead to an increase of the r_2/r_1 ratio (*i.e.* Figure 7), resulting in a diminished efficacy of the particles as T_1 contrast agents.

3.2.2. T_1-weighted MRI with SPION

For many years, and with the advent of synthetic methodologies enabling the preparation of small-sized and highly calibrated SPION[97,98], a great number of SPION-based contrast agents (Table 3) have been evaluated as potential T_1 contrast agents. The developed formulations differ in their synthetic procedures and in the various surface modifications used for the stabilization of the nanoparticles. Taupitz and coworkers initially explored preclinical studies about the potential of VSOP (Ferropharm) as T_1 contrast agents for MR angiography[56,57,61,99]. These pioneering studies demonstrated the potential of using SPION-based CAs for the investigation of coronary arteries. Moreover, VSOP was later shown to be suitable for tracking the evolution of atherosclerotic lesions at risk of destabilization[100]. Similar citrate coated 5 nm SPION were investigated by Taboada *et al.*[101]. These nanoparticles showed relaxivity values of r_1 = 14.5 $mM^{-1}s^{-1}$ and r_2 = 66.9 $mM^{-1}s^{-1}$ at 1.5 T.

In 2009, Tromsdorf *et al.* developed PEGylated iron oxide nanoparticles with various PEG chain lengths[102]. Authors demonstrated that a minimum PEG chain length with a molecular weight of 500 $g.mol^{-1}$ is required to provide stability to the nanoparticles in various buffer systems. SPION coated with PEG_{1100} exhibited a low r_2/r_1 ratio making them suitable as T_1 contrast agents for MRI. The low cytotoxicity as well as low unspecific cellular uptake into cells from the MPS (J774 mouse cells macrophages) was further evidenced. Similar PEGylated iron oxide nanoparticles were also developed by Hu *et al*. which obtained SPION with higher

relaxivities and smaller r_2/r_1 ratio, resulting in better contrast efficacy in both T_1-*w* and T_2-*w* images[103]. In 2011, Kim *et al*. investigated the magnetic and relaxometric properties of SPION with size varying between 1.5 and 3.7 nm as potential T_1 contrast agents. Size-dependent properties due to spin-canting effect were evaluated, small-sized SPION being characterized by low magnetic moments and almost paramagnetic field-dependent curves (Figure 13A & B). Their efficacy for high-resolution blood-pool imaging was demonstrated to be superior to Dotarem®, enabling the visualization of various blood vessels with size as low as 0.2 mm[104] (Figure 13C). In a later study, the same SPION were compared with manganese oxide nanoparticles and a clinically used GBCA (Gd-DTPA)[105]. The biosafety of each compound was evaluated on a mouse model. Results revealed a better safety profile for SPION resulting from their accumulation mostly occurring in the spleen, therefore inducing only stress related effect and no other severe damage.

In a similar study, Wang *et al.* developed PAA-coated SPION of 1.7, 2.2 and 4.6 nm with respective r_2/r_1 ratios of 2.03, 4.65 and 61.81 (at 7 T). The 2.2 nm SPION were evaluated as dual T_1-T_2 contrast agents and displayed good contrast enhancement, long-term circulation and low toxicity, which make them attractive for various clinical applications such as diagnosis of myocardial infarction, renal failure, atherosclerotic plaque, thrombosis and angiogenesis of tumor cells[106]. Furthermore, in 2014, Jung *et al*. demonstrated the feasibility of dual contrast-enhanced imaging using iron oxide nanoparticles as both T_1 and T_2 contrast agents for detecting vascular signals in MR angiography[107].

The same year, glutathione-capped iron oxide nanoparticles developed by Liu *et al*. were shown to have excellent dual contrast ability as well as biocompatibility[108]. *In vivo* results showed a strong enhancement in mouse's superior sagittal sinus, enabling the detection of cerebral arterial occlusions. Metabolization of the nanoparticles by kidneys was assessed by the

observed enhancement of the renal cortex, confirming the versatile potential of such systems for the study of renal disease or urinary tract tumor diagnosis.

Silica-coated iron oxide nanoparticles (SPION@SiO_2) as T_1 contrast agents were developed by Iqbal *et al*. in 2015[109]. The biocompatibility of SPION was enhanced using silica, yielding SPION@SiO_2 displaying r_1 and r_2 values of 1.2 $s^{-1}mM^{-1}$ and 7.8 $s^{-1}mM^{-1}$, respectively. *In vivo*, strong positive signal enhancement was observed in heart, liver, kidney and bladder. Another study from Hurley *et al*. showed the potential of silica-coated SPION for both positive contrast enhancement (using a SWIFT sequence *i.e.* SWept Imaging with Fourier Tranform) and hyperthermia treatment using intra-tumoral injection of these nanoparticles in prostate cancer tumors in nude mice[110].

Bhavesh *et al*. developed fluorescent dextran-coated iron oxide nanoparticles (fdIONP) with the use of microwave technology[111]. These nanoparticles showed relaxivity values of r_1 = 6 $s^{-1}mM^{-1}$ and r_2 = 27.9 $s^{-1}mM^{-1}$ (at 1.5 T) along with small hydrodynamic diameter of 21.5 nm. MRI and fluorescent phantom images were obtained with mouse adult fibroblasts incubated with increasing concentrations of iron (Figure 14A). The MRI positive contrast was further evidenced *in vivo* (Figure 14B) during CE-MRA experiments. A clear depiction of the main vascular architecture was maintained even 90 minutes post-injection.

In 2017, Shen *et al.* studied the relationship between the relaxivity values (r_1, r_2 and r_2/r_1 at 7 T) and the particle size[112]. SPION with various size were synthesized and a particle size of 3.6 nm was identified as the optimal one, combining ideal r_2/r_1 ratio and high r_1 value, for efficient positive contrast. A stimuli-responsive drug delivery system based on these SPION was then devised using dimeric RGD peptide (RGD_2) for tumor targeting, doxorubicine (DOX) as anticancer drug and PEG methyl ether (mPEG) grafted *via* an acid-labile-β-thiopropionate linker, enabling drug release in acidic tumor condition. T_1-weighted MR images recorded at different times after the administration of the nanoparticles *in vivo* demonstrated highest tumor

signal with the specific systems compared to unspecific ones (Magnevist® and 3.6 nm SPION without targeting vector).

Liang *et al*. developed an innovative SPION-based T_1 contrast agent based on zwitterionic SPION[113]. Zwitterionic dopamine sulfonate (ZDS) was used as stabilizer enabling the direct preparation of SPION (named ZUIONs) with a core size of 3.7 nm and a hydrodynamic size of 7 nm. Authors demonstrated the significant contrast enhancement induced *in vivo* by these systems as well as persistent intravascular circulation (over one hour), largely superior to the circulation time of Gd-DTPA, which was directly observed in the bladder 5 minutes post-injection (Figure 15). ZDS was more recently used by Liu *et al.* for the stabilization of hollow 7 nm and 10 nm SPION[114]. T_1 signal could be observed *in vivo* in a 4T1 xenograft mouse model on a 3 T scanner. Renal excretion of these ZDS-SPION was also assessed by both T_1 signal observed in the bladder but also by TEM analysis of the urine of mice showing the presence of the nanoparticles.

In 2019, Tao *et al.* performed a comparative study concerning the T_1 performance of SPION modified with either natural protein macromolecule (bovine serum albumin (BSA)) or an artificial molecule (poly(acrylic acid)-poly(methacrylic acid), PMAA-PTTM)[115]. Both systems displayed positive contrast enhancement *in vitro* on a 0.5 T MRI scanner. However, *in vivo* images showed opposite behaviors for the two types of SPION, BSA-coated nanoparticles showing negative contrast while positive contrast could be observed for PMMA-PTTM-coated nanoparticles. These observations, linked with differences in the stability of SPION, showed the importance of surface ligands on the performance of SPION as T_1 contrast agents.

Wang *et al.* demonstrated the feasibility of SPION-based contrast agent for ultrahigh field (UHF) ($\geq$ 7 T) T_1-weighted dynamic CE-MRI[116]. UHF MRI is particularly interesting in the case of CE-MRA for vessel visualization with higher spatial resolution and signal-to-noise ratio (SNR)[117]. Using extremely small superparamagnetic iron oxide nanoparticles (2.3 nm

SPION), clear visualization of microvascular anatomy was attained, providing a novel way for the medical diagnosis of vascular-related diseases. Our team also investigated the feasibility of using SPION for UHF T_1-weighted CE-MRI[118,119]. Sub-5 nm superparamagnetic iron oxide nanoparticles (SPIO-5) coated with polyethylene glycol of different chain lengths (*i.e*. PEG-800, -2000 and -5000) were investigated as T_1 contrast agents at 9.4 T. Specifically, a follow-up of biodistribution and elimination pathways by T_1- and T_2-weighted MRI as well as by optoacoustic imaging through the presence of a near-infrared-emitting dye (NIR-dye) onto the particle surface. Interestingly, differences in the pharmacokinetic properties could be observed depending on the thickness of the PEG coating, SPIO-5 bearing longer chains of PEG showing a persistent T_1 signal in cardiac left ventricle for several hours while SPIO-5-PEG_{800} were washed out within an hour (Figure 16).

Other than pure iron oxide nanoparticles, hybrid nanoparticles containing various metals such as europium (Eu), copper (Cu) or manganese (Mn), having enhanced T_1 signal, have been developed in the past years. For instance, Fernandez-Barahona *et al*. developed Cu-doped SPION displaying very large longitudinal relaxivity values and demonstrated their suitability for *in vivo* use in angiography as well as targeted molecular imaging[120]. However, even if such strategy has proven to yield systems exhibiting enhanced positive contrast, this must be weighed against the additional toxicity potentially induced by the dopants as well as the increased complexity required to achieve their synthesis[95].

4. General conclusions

Since the advent of MRI as a powerful imaging modality in clinical radiology practices, SPION have always hold great promises as contrast agents due to a combination of favorable attributes, namely their superparamagnetic properties, biocompatibility and their ease of surface modification with various coatings. Overall, this chapter provides an overview of the theoretical basis (SPM model) of the use of SPION as MRI contrast agents and (pre)clinical applications.

Although a substantial amount of work has been performed towards the translation of several SPION formulations into clinical applications, all the developed contrast agents didn't met the expected outcome and were withdrawn as a result of safety concern and/or lack of profit. Still, despite these pitfalls, SPION still show enormous potential as the next generation MRI contrast agents.

For many years, a particular emphasis is placed on the use of SPION-based T_1 contrast agents as potential alternatives to conventional GBCA, as a consequence of issues faced by the latter regarding their safety. Literature has clearly evidenced the excellent imaging performance of SPION as T_1 contrast agents for applications such as CE-MRA or targeted molecular imaging. However, much research has yet to be done to advance beyond-of-concept studies and to reach suitable SPION-based T_1 contrast agent yet to be developed to a clinical setting.

Abbreviations and definitions

CE-MRA	Contrast-Enhanced Magnetic Resonance Angiography
CE-MRI	Contrast-Enhanced Magnetic Resonance Imaging
GBCA	Gadolinium-based Contrast Agents
MPI	Magnetic Particle Imaging
MRI	Magnetic Resonance Imaging
NMR	Nuclear magnetic resonance
NMRD (profiles)	Nuclear magnetic resonance dispersion (profiles)
PEG	Polyethylene Glycol
SNR	Signal-to-Noise Ratio
SPION	SuperParamagnetic Iron Oxide Nanoparticle

T_1	Longitudinal relaxation time
T_2	Transverse relaxation time
UHF	Ultra-High Field
ZDS	Zwitterionic dopamine sulfonate

References

1. Huber, D. Synthesis, Properties, and Applications of Iron Nanoparticles. *Small* **2005**, *1*, 482–501.
2. Faivre, D. *Iron Oxides: From Nature to Applications*; 2nd completely rev. and extended ed.; Wiley-VCH: Weinheim ; New York, 2016; ISBN 978-3-527-29669-9.
3. Lam, U.T.; Mammucari, R.; Suzuki, K.; Foster, N.R. Processing of Iron Oxide Nanoparticles by Supercritical Fluids. *Ind. Eng. Chem. Res.* **2008**, *47*, 599–614.
4. Nguyen, M.D.; Tran, H.-V.; Xu, S.; Lee, T.R. Fe3O4 Nanoparticles: Structures, Synthesis, Magnetic Properties, Surface Functionalization, and Emerging Applications. *Appl. Sci.* **2021**, *11*, 11301, doi:10.3390/app112311301.
5. Issa, B.; M. Obaidat, I. Magnetic Nanoparticles as MRI Contrast Agents. In *Magnetic Resonance Imaging*; Manchev, L., Ed.; IntechOpen, 2019.
6. Estelrich, J.; Escribano, E.; Queralt, J.; Busquets, M. Iron Oxide Nanoparticles for Magnetically-Guided and Magnetically-Responsive Drug Delivery. *Int. J. Mol. Sci.* **2015**, *16*, 8070–8101.
7. Wahajuddin; Arora Superparamagnetic Iron Oxide Nanoparticles: Magnetic Nanoplatforms as Drug Carriers. *Int. J. Nanomedicine* **2012**, 3445–3471, doi:10.2147/IJN.S30320.
8. Malhotra, N.; Lee, J.-S.; Liman, R.A.D.; Ruallo, J.M.S.; Villaflores, O.B.; Ger, T.-R.; Hsiao, C.-D. Potential Toxicity of Iron Oxide Magnetic Nanoparticles: A Review. *Molecules* **2020**, *25*, 3159, doi:10.3390/molecules25143159.
9. Tietze, R.; Zaloga, J.; Unterweger, H.; Lyer, S.; Friedrich, R.P.; Janko, C.; Pöttler, M.; Dürr, S.; Alexiou, C. Magnetic Nanoparticle-Based Drug Delivery for Cancer Therapy. *Biochem. Biophys. Res. Commun.* **2015**, *468*, 463–470.
10. Ulbrich, K.; Holá, K.; Šubr, V.; Bakandritsos, A.; Tuček, J.; Zbořil, R. Targeted Drug Delivery with Polymers and Magnetic Nanoparticles: Covalent and Noncovalent Approaches, Release Control, and Clinical Studies. *Chem. Rev.* **2016**, *116*, 5338–5431.
11. Vangijzegem, T.; Stanicki, D.; Laurent, S. Magnetic Iron Oxide Nanoparticles for Drug Delivery: Applications and Characteristics. *Expert Opin. Drug Deliv.* **2019**, *16*, 69–78.
12. Palanisamy, S.; Wang, Y.-M. Superparamagnetic Iron Oxide Nanoparticulate System: Synthesis, Targeting, Drug Delivery and Therapy in Cancer. *Dalton Trans.* **2019**, *48*, 9490–9515.
13. Stanicki, D.; Vangijzegem, T.; Ternad, I.; Laurent, S. An Update on the Applications and Characteristics of Magnetic Iron Oxide Nanoparticles for Drug Delivery. *Expert Opin. Drug Deliv.* **2022**, *19*, 321–335, doi:10.1080/17425247.2022.2047020.
14. Jasmin; Torres, A.L.M.; Jelicks, L.; de Carvalho, A.C.C.; Spray, D.C.; Mendez-Otero, R. Labeling Stem Cells with Superparamagnetic Iron Oxide Nanoparticles: Analysis of the Labeling Efficacy by Microscopy and Magnetic Resonance Imaging. In *Nanoparticles in*

Biology and Medicine; Soloviev, M., Ed.; Humana Press: Totowa, NJ, 2012; Vol. 906, pp. 239–252.
15. Li, L.; Jiang, W.; Luo, K.; Song, H.; Lan, F.; Wu, Y.; Gu, Z. Superparamagnetic Iron Oxide Nanoparticles as MRI Contrast Agents for Non-Invasive Stem Cell Labeling and Tracking. *Theranostics* **2013**, *3*, 595–615.
16. Wang, Y.; Xu, C.; Ow, H. Commercial Nanoparticles for Stem Cell Labeling and Tracking. *Theranostics* **2013**, *3*, 544–560.
17. Stanicki, D.; Boutry, S.; Laurent, S.; Wacheul, L.; Nicolas, E.; Crombez, D.; Vander Elst, L.; Lafontaine, D.L.J.; Muller, R.N. Carboxy-Silane Coated Iron Oxide Nanoparticles: A Convenient Platform for Cellular and Small Animal Imaging. *J Mater Chem B* **2014**, *2*, 387–397.
18. Hedayatnasab, Z.; Abnisa, F.; Daud, W.M.A.W. Review on Magnetic Nanoparticles for Magnetic Nanofluid Hyperthermia Application. *Mater. Des.* **2017**, *123*, 174–196, doi:10.1016/j.matdes.2017.03.036.
19. Obaidat, I.; Issa, B.; Haik, Y. Magnetic Properties of Magnetic Nanoparticles for Efficient Hyperthermia. *Nanomaterials* **2015**, *5*, 63–89.
20. Kami, D.; Takeda, S.; Itakura, Y.; Gojo, S.; Watanabe, M.; Toyoda, M. Application of Magnetic Nanoparticles to Gene Delivery. *Int. J. Mol. Sci.* **2011**, *12*, 3705–3722.
21. Mulens, V.; Morales, M. del P.; Barber, D.F. Development of Magnetic Nanoparticles for Cancer Gene Therapy: A Comprehensive Review. *ISRN Nanomater.* **2013**, *2013*, 1–14.
22. Ziv-Polat, O.; Margel, S.; Shahar, A. Application of Iron Oxide Nanoparticles in Neuronal Tissue Engineering. *Neural Regen. Res.* **2015**, *10*, 189–191.
23. Nanda, T.; Alobaid, M.; Rege, K. Iron Oxide Nanoparticles for Tissue Repair and Regeneration. *Nano LIFE* **2021**, *11*, 2030001.
24. Bulte, J.W.M. Superparamagnetic Iron Oxides as MPI Tracers: A Primer and Review of Early Applications. *Adv. Drug Deliv. Rev.* **2019**, *138*, 293–301, doi:10.1016/j.addr.2018.12.007.
25. Hauser, A.K.; Mitov, M.I.; Daley, E.F.; McGarry, R.C.; Anderson, K.W.; Hilt, J.Z. Targeted Iron Oxide Nanoparticles for the Enhancement of Radiation Therapy. *Biomaterials* **2016**, *105*, 127–135, doi:10.1016/j.biomaterials.2016.07.032.
26. Kwatra, D.; Venugopal, A.; Anant, S. Nanoparticles in Radiation Therapy: A Summary of Various Approaches to Enhance Radiosensitization in Cancer. *Transl. Cancer Res.* **2013**, *2*, 13.
27. Ternad, I.; Penninckx, S.; Lecomte, V.; Vangijzegem, T.; Conrard, L.; Lucas, S.; Heuskin, A.-C.; Michiels, C.; Muller, R.N.; Stanicki, D.; et al. Advances in the Mechanistic Understanding of Iron Oxide Nanoparticles' Radiosensitizing Properties. *Nanomaterials* **2023**, *13*, 201, doi:10.3390/nano13010201.
28. Roch, A.; Muller, R.N.; Gillis, P. Theory of Proton Relaxation Induced by Superparamagnetic Particles. *J. Chem. Phys.* **1999**, *110*, 5403–5411.
29. Roch, A.; Gillis, P.; Ouakssim, A.; Muller, R.N. Proton Magnetic Relaxation in Superparamagnetic Aqueous Colloids: A New Tool for the Investigation of Ferrite Crystal Anisotropy. *J. Magn. Magn. Mater.* **1999**, *201*, 77–79.
30. Vuong, Q.L.; Gillis, P.; Roch, A.; Gossuin, Y. Magnetic Resonance Relaxation Induced by Superparamagnetic Particles Used as Contrast Agents in Magnetic Resonance Imaging: A Theoretical Review. *Wiley Interdiscip. Rev. Nanomed. Nanobiotechnol.* **2017**, *9*, e1468.
31. Freed, J.H. Dynamic Effects of Pair Correlation Functions on Spin Relaxation by Translational Diffusion in Liquids. II. Finite Jumps and Independent T_1 Processes. *J. Chem. Phys.* **1978**, *68*, 4034–4037.

32. Ayant, Y.; Belorizky, E.; Aluzon, J.; Gallice, J. Calcul des densités spectrales résultant d'un mouvement aléatoire de translation en relaxation par interaction dipolaire magnétique dans les liquides. *J. Phys.* **1975**, *36*, 991–1004.
33. De Marco, G.; Roch, A.; Peretti, I.; Gossuin, Y.; Lehmann, P.; Menuel, C.; Vallée, J.; Muller, R. Agents de contraste en IRM : approche théorique des mécanismes de relaxation. *Médecine Nucl.* **2006**, *30*, 645–658.
34. Gossuin, Y.; Gillis, P.; Hocq, A.; Vuong, Q.L.; Roch, A. Magnetic Resonance Relaxation Properties of Superparamagnetic Particles. *Wiley Interdiscip. Rev. Nanomed. Nanobiotechnol.* **2009**, *1*, 299–310.
35. Laurent, S.; Bridot, J.-L.; Elst, L.V.; Muller, R.N. Magnetic Iron Oxide Nanoparticles for Biomedical Applications. *Future Med. Chem.* **2010**, *2*, 427–449.
36. Gillis, P.; Koenig, S.H. Transverse Relaxation of Solvent Protons Induced by Magnetized Spheres: Application to Ferritin, Erythrocytes, and Magnetite. *Magn. Reson. Med.* **1987**, *5*, 323–345.
37. Roch, A.; Gossuin, Y.; Muller, R.N.; Gillis, P. Superparamagnetic Colloid Suspensions: Water Magnetic Relaxation and Clustering. *J. Magn. Magn. Mater.* **2005**, *293*, 532–539.
38. Vuong, Q.L.; Gillis, P.; Gossuin, Y. Monte Carlo Simulation and Theory of Proton NMR Transverse Relaxation Induced by Aggregation of Magnetic Particles Used as MRI Contrast Agents. *J. Magn. Reson.* **2011**, *212*, 139–148.
39. Matsumoto, Y.; Jasanoff, A. T_2 Relaxation Induced by Clusters of Superparamagnetic Nanoparticles: Monte Carlo Simulations. *Magn. Reson. Imaging* **2008**, *26*, 994–998.
40. Gupta, A.K.; Gupta, M. Synthesis and Surface Engineering of Iron Oxide Nanoparticles for Biomedical Applications. *Biomaterials* **2005**, *26*, 3995–4021.
41. Ali, A.; Zafar, H.; Zia, M.; ul Haq, I.; Phull, A.R.; Ali, J.S.; Hussain, A. Synthesis, Characterization, Applications, and Challenges of Iron Oxide Nanoparticles. *Nanotechnol. Sci. Appl.* **2016**, *9*, 49–67.
42. Wang, Y.-X.J.; Hussain, S.M.; Krestin, G.P. Superparamagnetic Iron Oxide Contrast Agents: Physicochemical Characteristics and Applications in MR Imaging. *Eur. Radiol.* **2001**, *11*, 2319–2331.
43. Morana, G. Contrast Agents for Hepatic MRI. *Cancer Imaging* **2007**, *7*, S24–S27, doi:10.1102/1470-7330.2007.9001.
44. Weissleder, R.; Stark, D.; Engelstad, B.; Bacon, B.; Compton, C.; White, D.; Jacobs, P.; Lewis, J. Superparamagnetic Iron Oxide: Pharmacokinetics and Toxicity. *Am. J. Roentgenol.* **1989**, *152*, 167–173.
45. Clément, O.; Siauve, N.; Cuénid, C.-A.; Frija, G. Liver Imaging with Ferumoxides (Feridex): Fundamentals, Controversies, and Practical Aspects. *Top. Magn. Reson. Imaging* **1998**, *9*, 167–182.
46. Ros, P.R.; Freeny, P.C.; Harms, S.E.; Seltzer, S.E.; Davis, P.L.; Chan, T.W.; Stillman, A.E.; Muroff, L.R.; Runge, V.M.; Nissembaum, M.A.; et al. Hepatic MR Imaging with Ferumoxides: A Multicenter Clinical Trial of the Safety and Efficacy in the Detection of Focal Hepatic Lesions. *Radiology* **1995**, *196*, 481–488.
47. Reimer, P.; Balzer, T. Ferucarbotran (Resovist): A New Clinically Approved RES-Specific Contrast Agent for Contrast-Enhanced MRI of the Liver: Properties, Clinical Development, and Applications. *Eur. Radiol.* **2003**, *13*, 1266–1276.
48. Reimer, P.; Schuierer, G.; Balzer, T.; Peters, P.E. Application of a Superparamagnetic Iron Oxide (Resovist®) for MR Imaging of Human Cerebral Blood Volume. *Magn. Reson. Med.* **1995**, *34*, 694–697.
49. Jung, C.W.; Jacobs, P. Physical and Chemical Properties of Superparamagnetic Iron Oxide MR Contrast Agents: Ferumoxides, Ferumoxtran, Ferumoxsil. *Magn. Reson. Imaging* **1995**, *13*, 661–674.

50. Heesakkers, R.A.M.; Hövels, A.M.; Jager, G.J. MRI with a Lymph-Node-Specific Contrast Agent as an Alternative to CT Scan and Lymph-Node Dissection in Patients with Prostate Cancer: A Prospective Multicohort Study. **2008**, *9*, 7.
51. Harisinghani, M.G.; Deserno, W.M. Noninvasive Detection of Clinically Occult Lymph-Node Metastases in Prostate Cancer. *N. Engl. J. Med.* **2003**, *348*, 2491–2499.
52. Corot, C.; Warlin, D. Superparamagnetic Iron Oxide Nanoparticles for MRI: Contrast Media Pharmaceutical Company R&D Perspective. **2013**, *5*, 12.
53. Fortuin, A.S.; Brüggemann, R.; Linden, J.; Panfilov, I.; Israël, B.; Scheenen, T.W.J.; Barentsz, J.O. Ultra-small Superparamagnetic Iron Oxides for Metastatic Lymph Node Detection: Back on the Block. *WIREs Nanomedicine Nanobiotechnology* **2018**, *10*, doi:10.1002/wnan.1471.
54. Kellar, K.E.; Fujii, D.K.; Gunther, W.H.H.; Briley-S, K.; Koenig, S.H. NC100150 Injection, a Preparation of Optimized Iron Oxide Nanoparticles for Positive-Contrast MR Angiography. *J. Magn. Reson. Imaging 11*, 488–494.
55. Schnorr, J.; Wagner, S.; Pilgrimm, H.; Hamm, B.; Taupitz, M. Preclinical Characterization of Monomer-Stabilized Very Small Superparamagnetic Iron Oxide Particles (VSOP) as a Blood Pool Contrast Medium for MR Angiography. *Acad. Radiol.* **2002**, *9*, S307–S309.
56. Schnorr, J.; Wagner, S.; Abramjuk, C.; Wojner, I.; Schink, T.; Kroencke, T.J.; Schellenberger, E.; Hamm, B.; Pilgrimm, H.; Taupitz, M. Comparison of the Iron Oxide-Based Blood-Pool Contrast Medium VSOP-C184 With Gadopentetate Dimeglumine for First-Pass Magnetic Resonance Angiography of the Aorta and Renal Arteries in Pigs. *Invest. Radiol.* **2004**, *39*, 546–553.
57. Taupitz, M.; Wagner, S.; Pilgrimm, H.; Hamm, B. New Generation of Monomer-Stabilized Very Small Superparamagnetic Iron Oxide Particles (VSOP) as Contrast Medium for MR Angiography: Preclinical Results in Rats and Rabbits. *J. Magn. Reson. Imaging* **2000**, *12*, 905–911.
58. Bachmann, R.; Conrad, R.; Kreft, B.; Luzar, O.; Block, W.; Flacke, S.; Pauleit, D.; Träber, F.; Gieseke, J.; Saebo, K.; et al. Evaluation of a New Ultrasmall Superparamagnetic Iron Oxide Contrast Agent Clariscan®, (NC100150) for MRI of Renal Perfusion: Experimental Study in an Animal Model: Evaluation of USPIO Contrast Agent NC100150, Clariscan®. *J. Magn. Reson. Imaging* **2002**, *16*, 190–195, doi:10.1002/jmri.10149.
59. Ittrich, H.; Peldschus, K.; Raabe, N.; Kaul, M.; Adam, G. Superparamagnetic Iron Oxide Nanoparticles in Biomedicine: Applications and Developments in Diagnostics and Therapy. *RöFo - Fortschritte Auf Dem Geb. Röntgenstrahlen Bildgeb. Verfahr.* **2013**, *185*, 1149–1166, doi:10.1055/s-0033-1335438.
60. Klein, C.; Nagel, E.; Schnackenburg, B.; Bornstedt, A.; Schalla, S.; Hoffmann, V.; Lehning, A.; Fleck, E. The Intravascular Contrast Agent Clariscan™ (NC 100150 Injection) for 3D MR Coronary Angiography in Patients with Coronary Artery Disease. *Magn. Reson. Mater. Phys.* **2000**, 3.
61. Taupitz, M.; Wagner, S.; Schnorr, J.; Kravec, I.; Pilgrimm, H.; Bergmann-Fritsch, H.; Hamm, B. Phase I Clinical Evaluation of Citrate-Coated Monocrystalline Very Small Superparamagnetic Iron Oxide Particles as a New Contrast Medium for Magnetic Resonance Imaging. *Invest. Radiol.* **2004**, *39*, 394–405.
62. Leiner, T.; Ho, K.Y.J.A.M.; Ho, V.B.; Bongartz, G.; Mali, W.P.T.M.; Rasch, W.; Van Engelshoven, J.M.A. Multicenter Phase-II Trial of Safety and Efficacy of NC100150 for Steady-State Contrast-Enhanced Peripheral Magnetic Resonance Angiography. *Eur. Radiol.* **2003**, *13*, 1620–1627, doi:10.1007/s00330-002-1791-6.
63. Wagner, M.; Wagner, S.; Schnorr, J.; Schellenberger, E.; Kivelitz, D.; Krug, L.; Dewey, M.; Laule, M.; Hamm, B.; Taupitz, M. Coronary MR Angiography Using Citrate-Coated

Very Small Superparamagnetic Iron Oxide Particles as Blood-Pool Contrast Agent: Initial Experience in Humans. *J. Magn. Reson. Imaging* **2011**, *34*, 816–823.
64. Wang, Y.-X.J. Current Status of Superparamagnetic Iron Oxide Contrast Agents for Liver Magnetic Resonance Imaging. *World J. Gastroenterol.* **2015**, *21*, 13400.
65. Lu, M.; Cohen, M.H.; Rieves, D.; Pazdur, R. FDA Report: Ferumoxytol for Intravenous Iron Therapy in Adult Patients with Chronic Kidney Disease. *Am. J. Hematol.* **2010**, *85*, 315–319.
66. Barton Pai, A.; Garba Ferumoxytol: A Silver Lining in the Treatment of Anemia of Chronic Kidney Disease or Another Dark Cloud? *J. Blood Med.* **2012**, *3*, 77–85.
67. Balakrishnan, V.S.; Rao, M.; Kausz, A.T.; Brenner, L.; Pereira, B.J.G.; Frigo, T.B.; Lewis, J.M. Physicochemical Properties of Ferumoxytol, a New Intravenous Iron Preparation. *Eur J Clin Invest* **2009**, *39*, 489–496.
68. Bashir, M.R.; Bhatti, L.; Marin, D.; Nelson, R.C. Emerging Applications for Ferumoxytol as a Contrast Agent in MRI: Emerging Applications of Ferumoxytol. *J. Magn. Reson. Imaging* **2015**, *41*, 884–898.
69. Toth, G.B.; Varallyay, C.G.; Horvath, A.; Bashir, M.R.; Choyke, P.L.; Daldrup-Link, H.E.; Dosa, E.; Finn, J.P.; Gahramanov, S.; Harisinghani, M.; et al. Current and Potential Imaging Applications of Ferumoxytol for Magnetic Resonance Imaging. *Kidney Int.* **2017**, *92*, 47–66.
70. Lehrman, E.D.; Plotnik, A.N.; Hope, T.; Saloner, D. Ferumoxytol-Enhanced MRI in the Peripheral Vasculature. *Clin. Radiol.* **2019**, *74*, 37–50, doi:10.1016/j.crad.2018.02.021.
71. Hope, M.D.; Hope, T.A.; Zhu, C.; Faraji, F.; Haraldsson, H.; Ordovas, K.G.; Saloner, D. Vascular Imaging With Ferumoxytol as a Contrast Agent. *Am. J. Roentgenol.* **2015**, *205*, W366–W373, doi:10.2214/AJR.15.14534.
72. Huang, Y.; Hsu, J.C.; Koo, H.; Cormode, D.P. Repurposing Ferumoxytol: Diagnostic and Therapeutic Applications of an FDA-Approved Nanoparticle. *Theranostics* **2022**, *12*, 796–816, doi:10.7150/thno.67375.
73. Neuwelt, E.A.; Várallyay, C.G.; Manninger, S.; Solymosi, D.; Haluska, M.; Hunt, M.A.; Nesbit, G.; Stevens, A.; Jerosch-Herold, M.; Jacobs, P.M.; et al. The Potential of Ferumoxytol Nanoparticle Magnetic Resonance Imaging, Perfusion and Angiography in Central Nervous System Malignancy: A Pilot Study. *Neurosurgery* **2007**, *60*, 601–612, doi:10.1227/01.NEU.0000255350.71700.37.
74. Wáng, Y.X.J.; Idée, J.-M. A Comprehensive Literatures Update of Clinical Researches of Superparamagnetic Resonance Iron Oxide Nanoparticles for Magnetic Resonance Imaging. *Quant. Imaging Med. Surg.* **2017**, *7*, 88–122, doi:10.21037/qims.2017.02.09.
75. Zhou, Z.; Yang, L.; Gao, J.; Chen, X. Structure-Relaxivity Relationships of Magnetic Nanoparticles for Magnetic Resonance Imaging. *Adv. Mater.* **2019**, *31*, 1804567.
76. Estelrich, J.; Sánchez-Martín, M.J.; Busquets, M.A. Nanoparticles in Magnetic Resonance Imaging: From Simple to Dual Contrast Agents. *Int. J. Nanomedicine* **2015**, *10*, 1727–1741.
77. Javed, Y.; Akhtar, K.; Anwar, H.; Jamil, Y. MRI Based on Iron Oxide Nanoparticles Contrast Agents: Effect of Oxidation State and Architecture. *J. Nanoparticle Res.* **2017**, *19*, doi:10.1007/s11051-017-4045-x.
78. Na, H.B.; Hyeon, T. Nanostructured T1 MRI Contrast Agents. *J. Mater. Chem.* **2009**, *19*, 6267.
79. Bulte, J.W.M.; Kraitchman, D.L. Iron Oxide MR Contrast Agents for Molecular and Cellular Imaging. *NMR Biomed.* **2004**, *17*, 484–499.
80. Grobner, T. Gadolinium – a Specific Trigger for the Development of Nephrogenic Fibrosing Dermopathy and Nephrogenic Systemic Fibrosis? *Nephrol. Dial. Transplant.* **2006**, *21*, 1104–1108.

81. Grobner, T.; Prischl, F. Gadolinium and Nephrogenic Systemic Fibrosis. *Kidney Int.* **2007**, *72*, 260–264.
82. Idée, J.-M.; Port, M.; Medina, C.; Lancelot, E.; Fayoux, E.; Ballet, S.; Corot, C. Possible Involvement of Gadolinium Chelates in the Pathophysiology of Nephrogenic Systemic Fibrosis: A Critical Review. *Toxicology* **2008**, *248*, 77–88.
83. Do, C.; DeAguero, J.; Brearley, A.; Trejo, X.; Howard, T.; Escobar, G.P.; Wagner, B. Gadolinium-Based Contrast Agent Use, Their Safety, and Practice Evolution. *Kidney360* **2020**, *1*, 561–568, doi:10.34067/KID.0000272019.
84. Kanda, T.; Ishii, K.; Kawaguchi, H.; Kitajima, K.; Takenaka, D. High Signal Intensity in the Dentate Nucleus and Globus Pallidus on Unenhanced T_1-Weighted MR Images: Relationship with Increasing Cumulative Dose of a Gadolinium-Based Contrast Material. *Radiology* **2014**, *270*, 834–841.
85. Tedeschi, E.; Caranci, F.; Giordano, F.; Angelini, V.; Cocozza, S.; Brunetti, A. Gadolinium Retention in the Body: What We Know and What We Can Do. *Radiol. Med. (Torino)* **2017**, *122*, 589–600.
86. Kanda, T.; Fukusato, T.; Matsuda, M.; Toyoda, K.; Oba, H.; Kotoku, J.; Haruyama, T.; Kitajima, K.; Furui, S. Gadolinium-Based Contrast Agent Accumulates in the Brain Even in Subjects without Severe Renal Dysfunction: Evaluation of Autopsy Brain Specimens with Inductively Coupled Plasma Mass Spectroscopy. *Radiology* **2015**, *276*, 228–232.
87. Gulani, V.; Calamante, F.; Shellock, F.G.; Kanal, E.; Reeder, S.B. Gadolinium Deposition in the Brain: Summary of Evidence and Recommendations. *Lancet Neurol.* **2017**, *16*, 564–570.
88. Malikova, H.; Holesta, M. Gadolinium Contrast Agents - Are They Really Safe? *J. Vasc. Access* **2017**, *18*, 1–7.
89. Bao, Y.; Sherwood, J.; Sun, Z. Magnetic Iron Oxide Nanoparticles as T1 Contrast Agents for Magnetic Resonance Imaging. *J. Mater. Chem. C* **2018**, *6*, 1280–1290.
90. Caspani, S.; Magalhães, R.; Araújo, J.P.; Sousa, C.T. Magnetic Nanomaterials as Contrast Agents for MRI. **2020**, 37.
91. Fernández-Barahona, I.; Muñoz-Hernando, M.; Ruiz-Cabello, J.; Herranz, F.; Pellico, J. Iron Oxide Nanoparticles: An Alternative for Positive Contrast in Magnetic Resonance Imaging. *Inorganics* **2020**, *8*, 28, doi:10.3390/inorganics8040028.
92. Coey, J.M.D. Noncollinear Spin Arrangement in Ultrafine Ferrimagnetic Crystallites. *Phys. Rev. Lett.* **1971**, *27*, 1140–1142.
93. Linderoth, S.; Hendriksen, P.V.; Bo/dker, F.; Wells, S.; Davies, K.; Charles, S.W.; Mo/rup, S. On Spin-canting in Maghemite Particles. *J. Appl. Phys.* **1994**, *75*, 6583–6585.
94. Mohapatra, J.; Xing, M.; Liu, J.P. Inductive Thermal Effect of Ferrite Magnetic Nanoparticles. *Materials* **2019**, *12*, 3208, doi:10.3390/ma12193208.
95. Jeon, M.; Halbert, M.V.; Stephen, Z.R.; Zhang, M. Iron Oxide Nanoparticles as T_1 Contrast Agents for Magnetic Resonance Imaging: Fundamentals, Challenges, Applications, and Prospectives. *Adv. Mater.* **2020**, 1906539, doi:10.1002/adma.201906539.
96. Morales, M.P.; Veintemillas-Verdaguer, S.; Montero, M.I.; Serna, C.J.; Roig, A.; Casas, Ll.; Martínez, B.; Sandiumenge, F. Surface and Internal Spin Canting in γ-Fe_2O_3 Nanoparticles. *Chem. Mater.* **1999**, *11*, 3058–3064.
97. Stanicki, D.; Elst, L.V.; Muller, R.N.; Laurent, S. Synthesis and Processing of Magnetic Nanoparticles. *Curr. Opin. Chem. Eng.* **2015**, *8*, 7–14, doi:10.1016/j.coche.2015.01.003.
98. Avasthi, A.; Caro, C.; Garcia-Martin, M.L.; Pernia Leal, M. Deciphering the Parameters to Produce Highly Reproducible and Scalable Iron Oxide Nanoparticles. *React. Chem. Eng.* **2023**, 10.1039.D2RE00516F, doi:10.1039/D2RE00516F.

99. Taupitz, M.; Schnorr, J.; Wagner, S.; Abramjuk, C.; Pilgrimm, H.; Kivelitz, D.; Schink, T.; Hansel, J.; Laub, G.; Hünigen, H.; et al. Coronary MR Angiography: Experimental Results with a Monomer-Stabilized Blood Pool Contrast Medium. *Radiology* **2002**, *222*, 120–126.
100. Taupitz, M.; Wagner; Schnorr; Ludwig; Stangl; Ebert; Hamm Contrast-Enhanced MR Imaging of Atherosclerosis Using Citrate-Coated Superparamagnetic Iron Oxide Nanoparticles: Calcifying Microvesicles as Imaging Target for Plaque Characterization. *Int. J. Nanomedicine* **2013**, *8*, 767–779, doi:10.2147/IJN.S38702.
101. Taboada, E.; Rodríguez, E.; Roig, A.; Oró, J.; Roch, A.; Muller, R.N. Relaxometric and Magnetic Characterization of Ultrasmall Iron Oxide Nanoparticles with High Magnetization. Evaluation as Potential T_1 Magnetic Resonance Imaging Contrast Agents for Molecular Imaging. *Langmuir* **2007**, *23*, 4583–4588.
102. Tromsdorf, U.I.; Bruns, O.T.; Salmen, S.C.; Beisiegel, U.; Weller, H. A Highly Effective, Nontoxic T_1 MR Contrast Agent Based on Ultrasmall PEGylated Iron Oxide Nanoparticles. *Nano Lett.* **2009**, *9*, 4434–4440.
103. Hu, F.; Jia, Q.; Li, Y.; Gao, M. Facile Synthesis of Ultrasmall PEGylated Iron Oxide Nanoparticles for Dual-Contrast T_1 - and T_2 -Weighted Magnetic Resonance Imaging. *Nanotechnology* **2011**, *22*, doi:10.1088/0957-4484/22/24/245604.
104. Kim, B.H.; Lee, N.; Kim, H.; An, K.; Park, Y.I.; Choi, Y.; Shin, K.; Lee, Y.; Kwon, S.G.; Na, H.B.; et al. Large-Scale Synthesis of Uniform and Extremely Small-Sized Iron Oxide Nanoparticles for High-Resolution T_1 Magnetic Resonance Imaging Contrast Agents. *J. Am. Chem. Soc.* **2011**, *133*, 12624–12631.
105. Chen, R.; Ling, D.; Zhao, L.; Wang, S.; Liu, Y.; Bai, R.; Baik, S.; Zhao, Y.; Chen, C.; Hyeon, T. Parallel Comparative Studies on Mouse Toxicity of Oxide Nanoparticle- and Gadolinium-Based T_1 MRI Contrast Agents. *ACS Nano* **2015**, *9*, 12425–12435.
106. Wang, G.; Zhang, X.; Skallberg, A.; Liu, Y.; Hu, Z.; Mei, X.; Uvdal, K. One-Step Synthesis of Water-Dispersible Ultra-Small Fe_3O_4 Nanoparticles as Contrast Agents for T_1 and T_2 Magnetic Resonance Imaging. *Nanoscale* **2014**, *6*, 2953–2963.
107. Jung, H.; Park, B.; Lee, C.; Cho, J.; Suh, J.; Park, J.; Kim, Y.; Kim, J.; Cho, G.; Cho, H. Dual MRI T_1 and $T_2(*)$ Contrast with Size-Controlled Iron Oxide Nanoparticles. *Nanomedicine Nanotechnol. Biol. Med.* **2014**, *10*, 1679–1689.
108. Liu, C.-L.; Peng, Y.-K.; Chou, S.-W.; Tseng, W.-H.; Tseng, Y.-J.; Chen, H.-C.; Hsiao, J.-K.; Chou, P.-T. One-Step, Room-Temperature Synthesis of Glutathione-Capped Iron-Oxide Nanoparticles and Their Application in *In Vivo* T_1-Weighted Magnetic Resonance Imaging. *Small* **2014**, *10*, 3962–3969.
109. Iqbal, M.Z.; Ma, X.; Chen, T.; Zhang, L.; Ren, W.; Wu, A. Silica Coated Super-Paramagnetic Iron Oxide Nanoparticles (SPIONPs): A New Type Contrast Agent of T_1 Magnetic Resonance Imaging (MRI). *J. Mater. Chem. B* **2015**, *3*, 5172–5181.
110. Hurley, K.R.; Ring, H.; Etheridge, M.L.; Zhang, J.; Shao, Q.; Klein, N.D.; Szlag, V.; Chung, C.; Reineke, M.; Garwood, M.G.; et al. Predictable Heating and Positive MRI Contrast from a Mesoporous Silica-Coated Iron Oxide Nanoparticle. *Mol. Pharm.* **2016**, *13*, 2172–2183.
111. Bhavesh, R.; Lechuga-Vieco, A.V.; Ruiz-Cabello, J.; Herranz, F. T_1-MRI Fluorescent Iron Oxide Nanoparticles by Microwave Assisted Synthesis. *Nanomaterials* **2015**, *5*, 1880–1890.
112. Shen, Z.; Chen, T.; Ma, X.; Ren, W.; Zhou, Z.; Zhu, G.; Zhang, A.; Liu, Y.; Song, J.; Li, Z.; et al. Multifunctional Theranostic Nanoparticles Based on Exceedingly Small Magnetic Iron Oxide Nanoparticles for T_1 -Weighted Magnetic Resonance Imaging and Chemotherapy. *ACS Nano* **2017**, *11*, 10992–11004.

113. Liang, G.; Han, J.; Hao, Q. Gram-Scale Preparation of Iron Oxide Nanoparticles with Renal Clearance Properties for Enhanced T_1-Weighted MR Imaging. *ACS Appl. Bio Mater.* **2018**, *1*, 1389–1397.
114. Liu, W.; Deng, G.; Wang, D.; Chen, M.; Zhou, Z.; Yang, H.; Yang, S. Renal-Clearable Zwitterionic Conjugated Hollow Ultrasmall Fe_3O_4 Nanoparticles for T_1 -Weighted MR Imaging *in Vivo*. *J. Mater. Chem. B* **2020**, *8*, 3087–3091.
115. Tao, C.; Zheng, Q.; An, L.; He, M.; Lin, J.; Tian, Q.; Yang, S. T_1-Weight Magnetic Resonance Imaging Performances of Iron Oxide Nanoparticles Modified with a Natural Protein Macromolecule and an Artificial Macromolecule. *Nanomaterials* **2019**, *9*, 11, doi:10.3390/nano9020170.
116. Wang, J.; Jia, Y.; Wang, Q.; Liang, Z.; Han, G.; Wang, Z.; Lee, J.; Zhao, M.; Li, F.; Bai, R.; et al. An Ultrahigh-Field-Tailored T_1–T_2 Dual-Mode MRI Contrast Agent for High-Performance Vascular Imaging. *Adv. Mater.* **2020**, *33*, doi:10.1002/adma.202004917.
117. Fries, P.; Morelli, J.N.; Lux, F.; Tillement, O.; Schneider, G.; Buecker, A. The Issues and Tentative Solutions for Contrast-Enhanced Magnetic Resonance Imaging at Ultra-High Field Strength. *Wiley Interdiscip. Rev. Nanomed. Nanobiotechnol.* **2014**, *6*, 559–573.
118. Vangijzegem, T.; Stanicki, D.; Boutry, S.; Paternoster, Q.; Vander Elst, L.; Muller, R.N.; Laurent, S. VSION as High Field MRI T $_1$ Contrast Agent: Evidence of Their Potential as Positive Contrast Agent for Magnetic Resonance Angiography. *Nanotechnology* **2018**, *29*, 265103, doi:10.1088/1361-6528/aabbd0.
119. Stanicki, D.; Larbanoix, L.; Boutry, S.; Vangijzegem, T.; Ternad, I.; Garifo, S.; Muller, R.N.; Laurent, S. Impact of the Chain Length on the Biodistribution Profiles of PEGylated Iron Oxide Nanoparticles: A Multimodal Imaging Study. *J. Mater. Chem. B* **2021**, *9*, 5055–5068, doi:10.1039/d1tb00573a.
120. Fernández-Barahona, I.; Gutiérrez, L.; Veintemillas-Verdaguer, S.; Pellico, J.; Morales, M.D.P.; Catala, M.; Del Pozo, M.A.; Ruiz-Cabello, J.; Herranz, F. Cu-Doped Extremely Small Iron Oxide Nanoparticles with Large Longitudinal Relaxivity: One-Pot Synthesis and in Vivo Targeted Molecular Imaging. *ACS Omega* **2019**, *4*, 2719–2727, doi:10.1021/acsomega.8b03004.

Tables

Table 1. Chemical and structural properties of hematite (α-Fe_2O_3), magnetite (Fe_3O_4) and maghemite (γ-Fe_2O_3)**[3]**.

Property	**Iron oxide phase**		
	Hematite	Magnetite	Maghemite
Molecular formula	α-Fe_2O_3	Fe_3O_4	γ-Fe_2O_3
Crystal structure	Rhomboedral, hexagonal	Cubic	Cubic
Density (g/cm^3)	5.26	5.18	4.87
Melting point (°C)	1350	1597	/
Boiling point (°C)	/	2623	/
Color	Red	Black	Reddish-brown
Hardness (Mohs scale)	6.5	5.5	5
Magnetic behavior	Weakly ferromagnetic or antiferromagnetic	Ferrimagnetic	Ferrimagnetic
Curie temperature (K)	956	850	820-986[1]
M_{SAT} at 300 K (A.m^2.kg^{-1})	0.3	92-100	76
Standard free energy of formation (ΔG_f^0) (kJ.mol^{-1})	-742.7	-1012.6	-711.1
Heat of decomposition (kJ.mol^{-1})	461.4	605	457.6

[1] Range due to thermal conversion of maghemite to hematite at temperatures below the Curie temperature.

Table 2. Generic, trade names and applications of SPION-based T_2 contrast agents.

Agent	**Generic name**	**Trade name**	**Application**
AMI-25	Ferumoxide	Endorem® Feridex®	Liver MRI
SHU 555A	Ferucarbotran	Resovist®	Liver MRI
AMI-227	Ferumoxtran-10	Sinerem® Combidex®	Lymph node MRI
NC100150	Feruglose	Clariscan®	Blood-pool MRI
VSOP C184	Ferropharm	/	Blood-pool MRI
AMI-121	Ferumoxsil	Lumirem®	Gastrointestinal MRI
OMP	Ferristene	Abdoscan®	Gastrointestinal MRI
/	Ferumoxytol	Feraheme®	Treatment of iron deficiency anemia

Table 3. Inorganic diameter, coating material, relaxivity values and ratios at corresponding magnetic fields of reported SPION-based T_1 contrast agents.

Coating	D_{TEM} (nm)	r_1 ($s^{-1}mM^{1}$)	r_2 ($s^{-1}mM^{-1}$)	r_2/r_1	Magnetic field (T)	Reference
Citrate	4.8 ± 0.6	14.5	66.9	4.61	1.5	[101]
PEG_{1100}	4	7.3	17.6	2.4	1.41	[102]
PEG_{600}	5.4 ± 0.7	19.7	39.5	2	1.5	[103]
Phosphine oxide-PEG	2.2 ± 0.4 3 ± 0.5 12	4.8 4.8 2.4	17.5 29.2 58.8	3.67 6.12 24.8	3	[104,105]
PAA	1.7 2.2 4.6	8.2 6.1 1.1	16.7 28.6 64.4	2.03 4.65 61.81	1.41	[106]
Dextran	7	13.3 6.8	40.9 39.7	3.07 5.84	1.43 3	[107]
Glutathione	3.7 ± 0.1	3.6	8.3	2.28	4.7	[108]
SiO_2	4 - 5	1.2	7.8	6.5	3	[109]
SiO_2-PEG	10 ± 2.5	6.9	~ 270	39.13	1.4	[110]
Dextran	2.5 ± 0.2	6	27.9	4.7	1.5	[111]
PAA-PEG	3.6	12.7	23.5	1.9	0.5	[112]
		8.8	22.7	2.6	1.5	
		2.3	24.4	10.5	7	
ZDS	3.7 ± 0.8	2.4	5.2	2.16	1	[113]
ZDS	7	0.2	0.9	4.5	0.5	[114]

	10	2.5	46.4	18.7		
BSA	5.3 ± 1.2	39.3	179.8	4.57	0.5	[115]
PMAA-PTTM	4.3 ± 1.5	24.2	67.2	2.77		
PEG	2.3	1.4	7.5	5.5	7	[116]
PEG_{750}	3.5 ± 0.6	12.7	19.7	1.55	0.5	[118]
		11	28.1	2.55	1.5	
PEG_{2000}		7.9	13	1.64	0.5	
		6.8	17.9	2.63	1.5	
PEG_{800}	4.8 ± 1	19.8	32.2	1.62	0.5	[119]
PEG_{2000}	4.8 ± 0.9	20.1	32.8	1.63		
PEG_{5000}	5 ± 1	19.9	32.8	1.65		

Figures

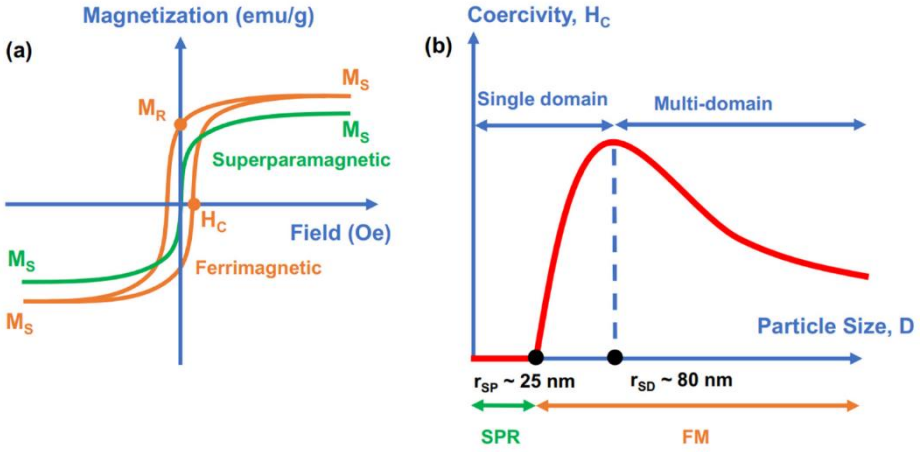

Figure 1. (a) Magnetization versus applied field (M–H) curves for superparamagnetic (green curve) and ferrimagnetic (FM) (orange curve) material and (b) relations between size, coercivity, and magnetic behavior. Reprinted with permission from **[4]**. Copyright 2021 MDPI Applied Sciences.

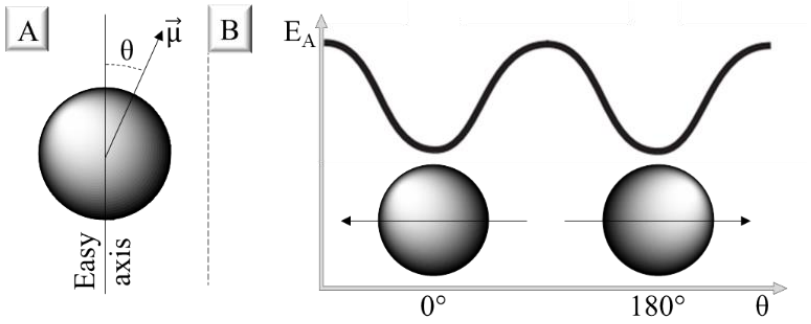

Figure 2. (A) Uniaxial anisotropy axis of spherical nanoparticle, θ is the angle between the magnetic moment ($\vec{\mu}$) and the easy axis; (B) Evolution of anisotropy energy with the angle between easy axis and magnetic moment.

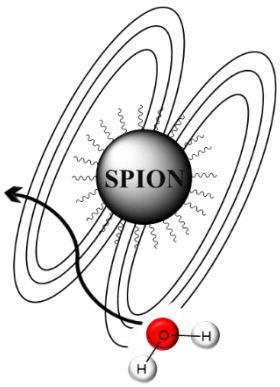

Figure 3. Illustration of the diffusion of water molecules through magnetic field inhomogeneities responsible for modification of proton relaxation rates.

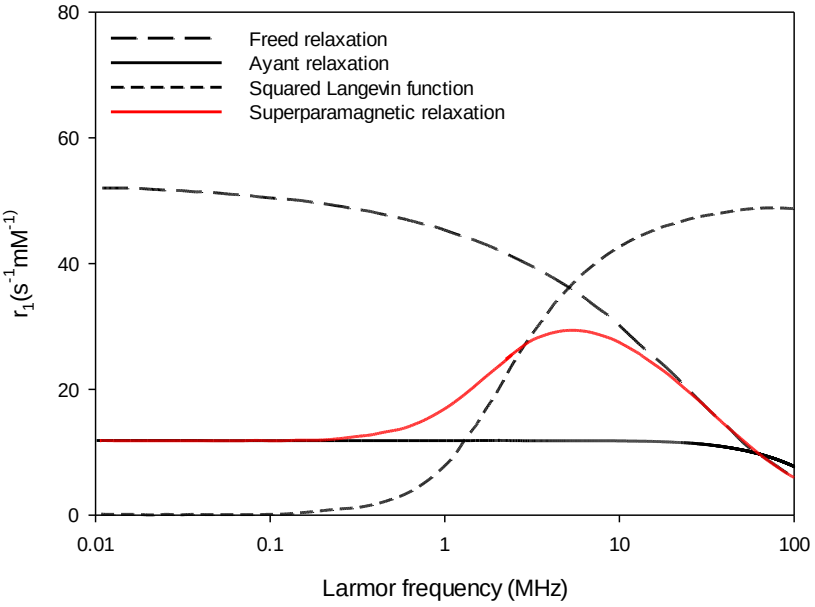

Figure 4. Illustration of field-dependent relaxation processes contributing to the global superparamagnetic relaxation of large crystals. Reproduced from **[33]**.

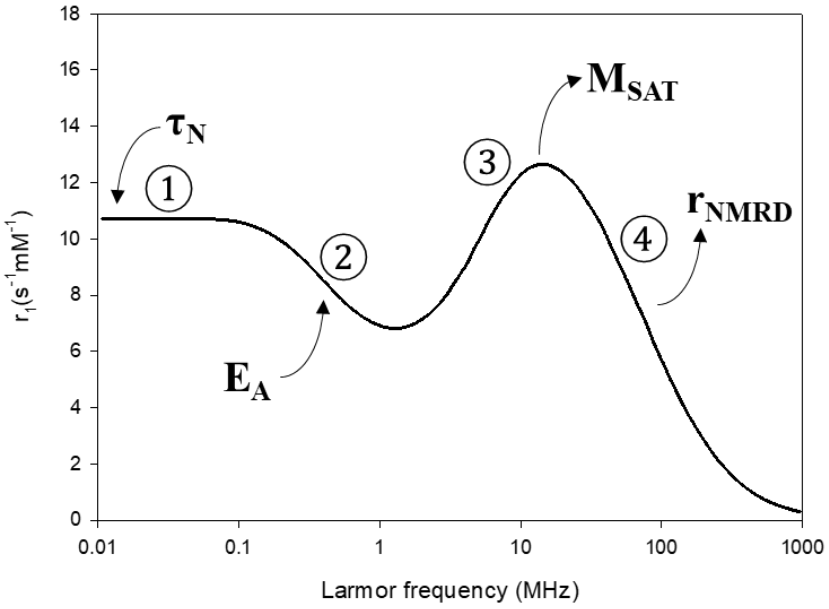

Figure 5. Theoritical NMRD curve of SPION with low anisotropy energy obtained by the RMG model and region of influence of the different physicochemical parameters of SPION.

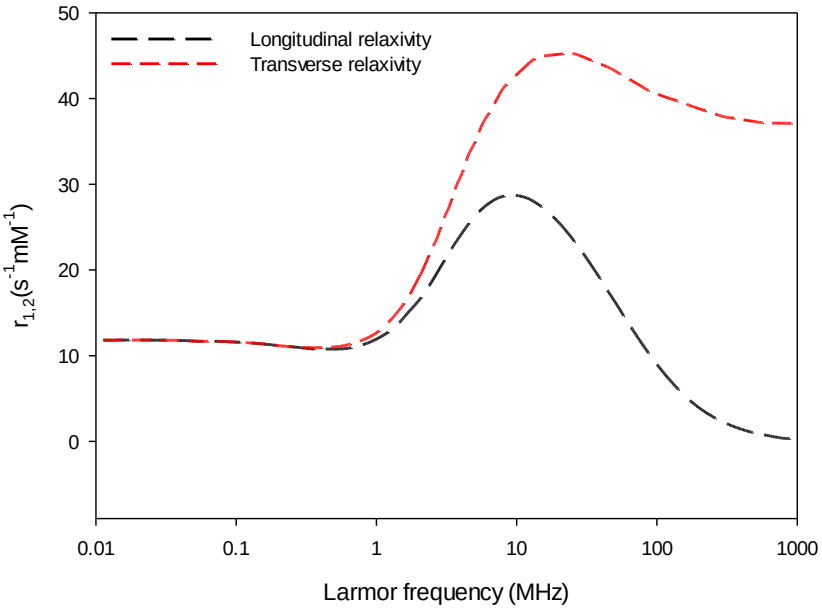

Figure 6. NMRD profiles for longitudinal and transverse relaxations of 10 nm superparamagnetic iron oxide nanoparticles.

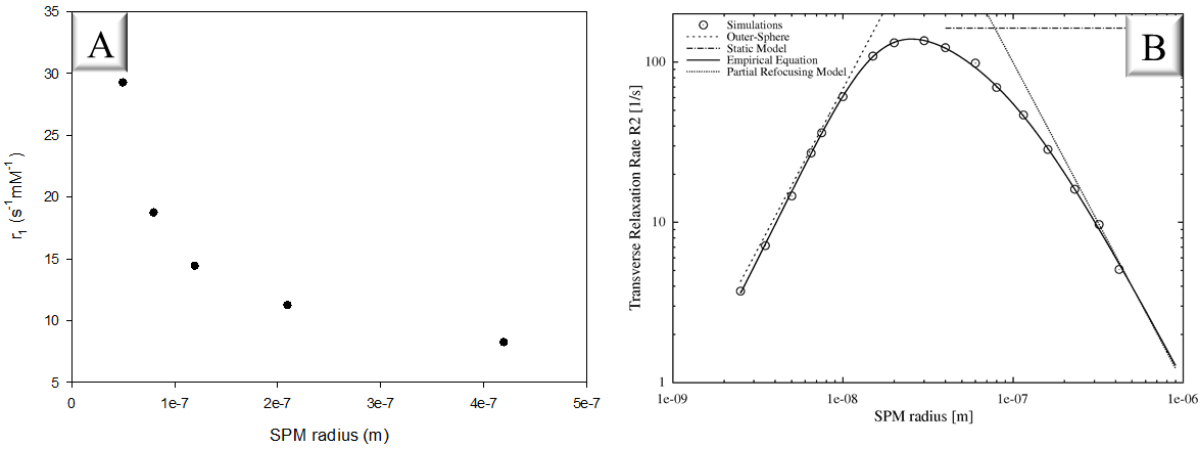

Figure 7. (A) Evolution of proton longitudinal relaxivity (at magnetic field of 20 MHz) as a function of nanoparticle agglomeration (data extracted from **[37]**); (B) Simulation results and theoretical predictions of the transverse relaxation rate at high magnetic field using various models (reprinted with permission from **[38]**). Copyright 2011 Elsevier)

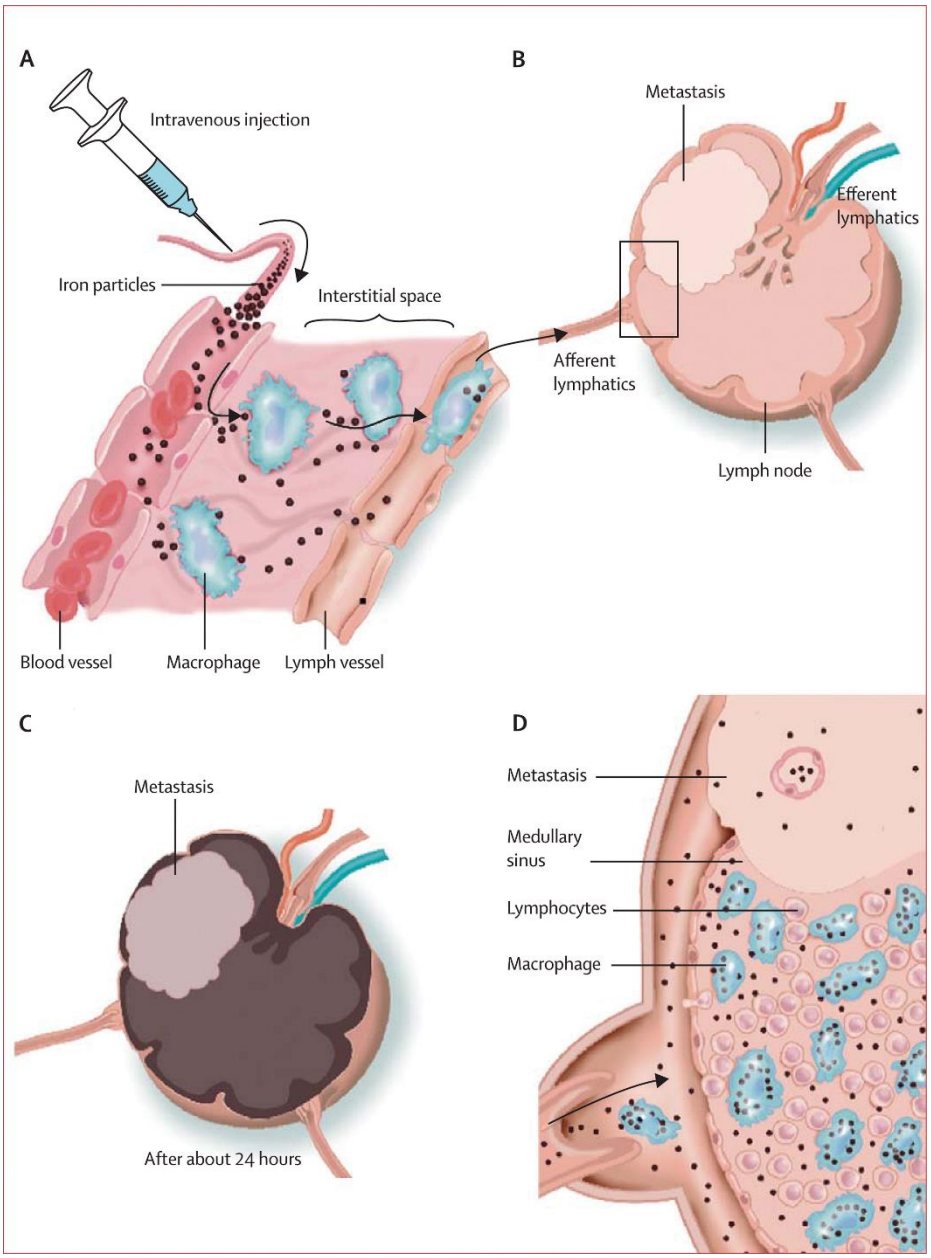

Figure 8. (A) Infused iron-particles slowly extravasate from the vascular to the interstitial space and are internalised by macrophages. (B) and (C) Iron-loaded macrophages are transported to lymph nodes via lymphatic vessels and accumulate in normal-sized lymph node tissue. These iron-loaded macrophages cause low signal intensity on T_2*-weighted MR image. Box in B shows area depicted in D. (D) Disturbances of lymph flow or nodal architecture by metastases leads to less macrophages, depicted at MR imaging by higher signal intensity. Reprinted with permission from **[50]**. Copyright 2008 Elsevier.

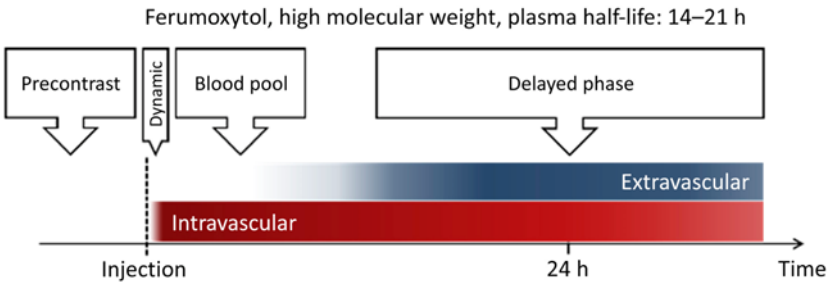

Figure 9. Phases of Ferumoxytol enhancement. Reprinted with permission from **[69]**. Copyright 2017 Elsevier.

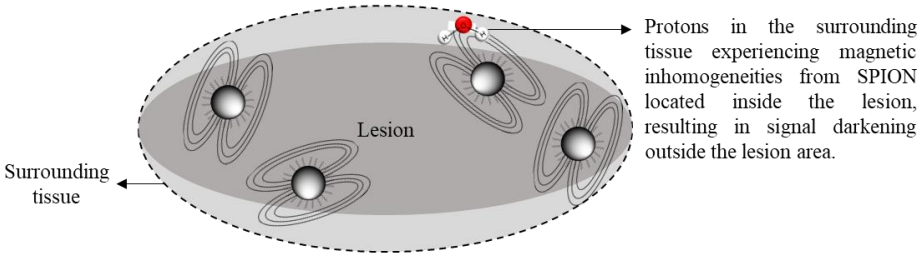

Figure 10. Schematical illustration of the blooming effect, causing the overestimation of lesion size due to SPION located inside the lesion inducing relaxation of protons in the surrounding tissue.

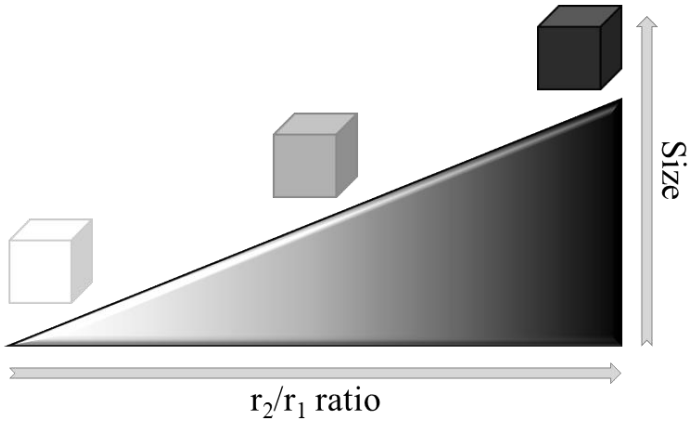

Figure 11. Influence of the r_2/r_1 ratio on the efficacy of a contrast agent. Reproduced from **[76]** Originally published by and used with permission from Dove Medical Press Ltd..

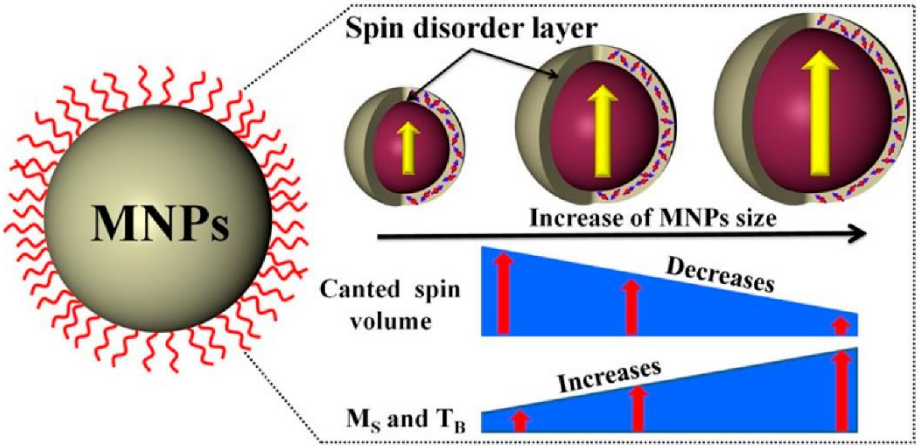

Figure 12. Schematic representation of the variation of spin-canting effect, saturation magnetization, and blocking temperature with the MNPs size. Reprinted with permission from **[94]**. Copyright 2019 MDPI Materials.

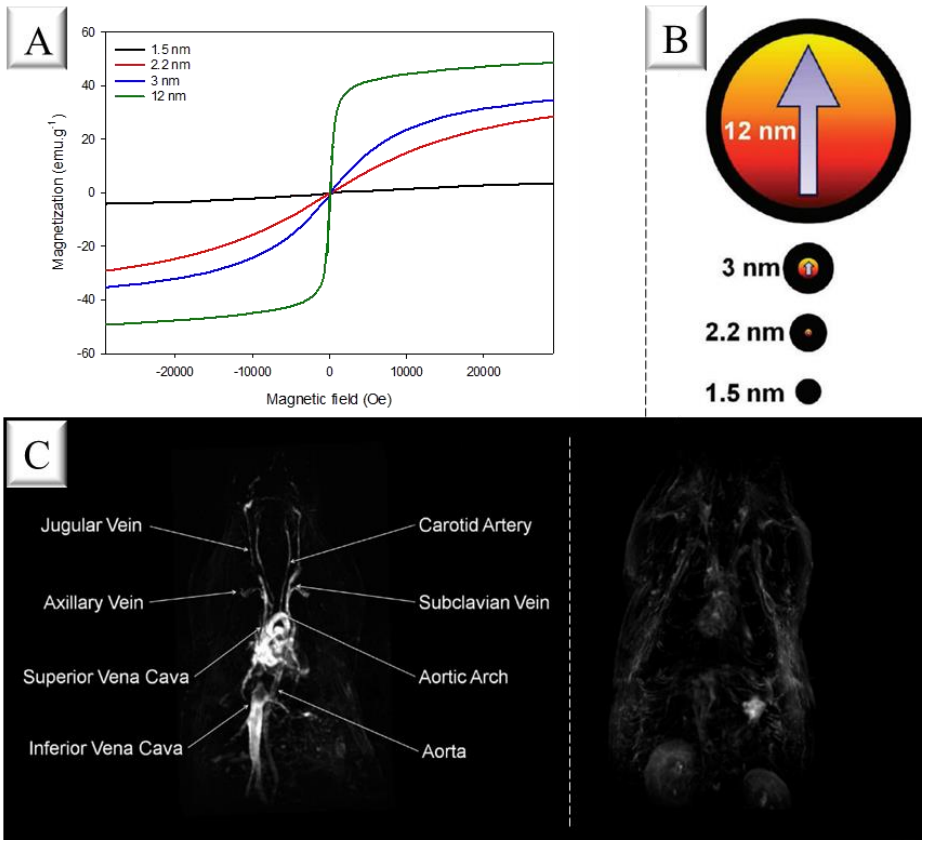

Figure 13. (A) Field-dependent magnetization curves for SPION with various diameter; (B) Illustration of the size-dependent spin-canting effect in iron oxide nanoparticles with various diameters; (C) Comparison of *in vivo* blood-pool images obtained with a 3d-FLASH sequence using 3 nm SPION (left) and Dotarem (right). Adapted with permission from **[104]**. Copyright 2011 American Chemical Society.

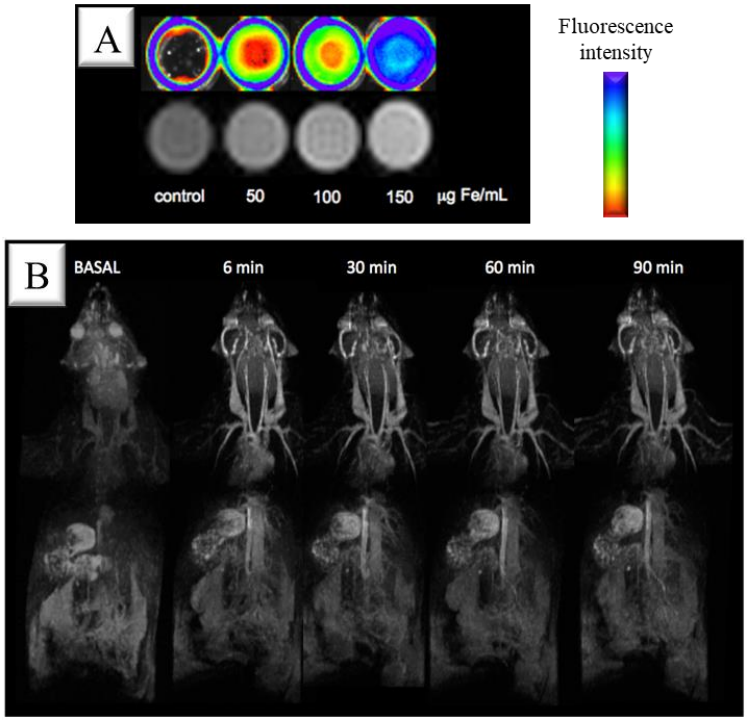

Figure 14. (A) *In vitro* phantom images (top-row: fluorescence phantoms; bottom-row: MRI phantoms) of mouse adult fibroblasts incubated with increasing concentrations of fdIONP; (B) *In vivo* CE-MRA images before and after administration of fdIONP at increasing times. Reprinted from **[111]**. Copyright 2015 MPDI Nanomaterials.

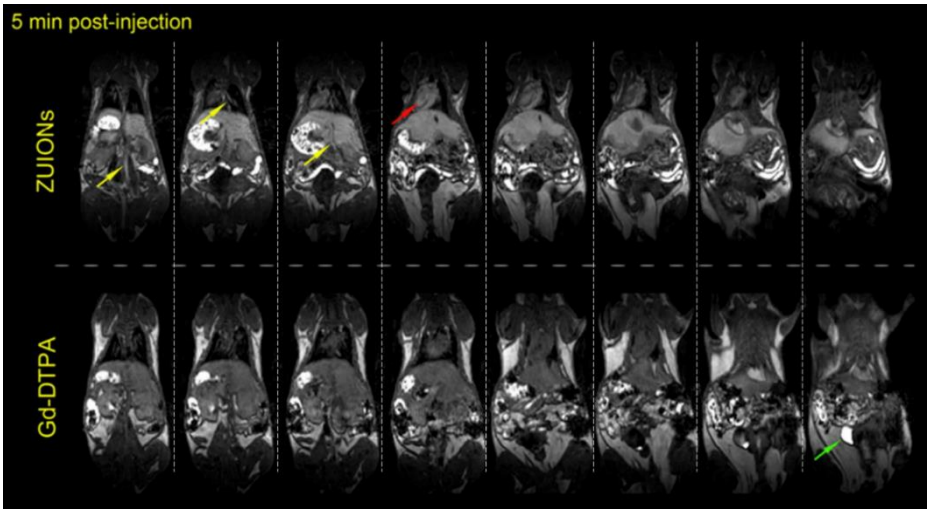

Figure 15. MRI slices (slice thickness = 0.8 mm) of mice at 5 min post-injection of ZUIONs (0.041 mmol $Fe.kg^{-1}$) or Gd-DTPA (0.041 mmol $Gd.kg^{-1}$) showing signal enhancement in blood vessels (yellow arrow), heart (red arrow) and bladder (green arrow), the latter one observed for the injection of Gd-DTPA only. Reprinted with permission from **[113]**. Copyright 2018 American Chemical Society.

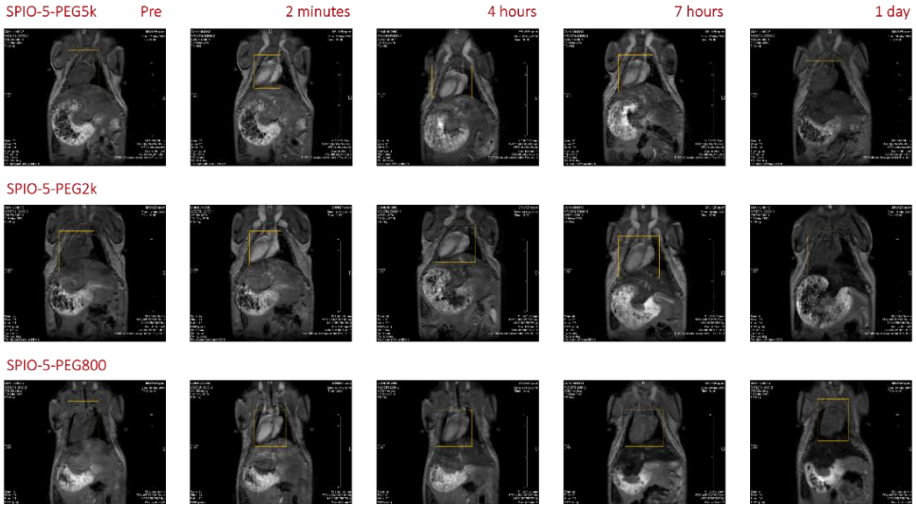

Figure 16. Illustration of *in vivo* MRI data collected on mice treated with the different types of SPIO-5 at a dose of 70 mmol Fe.kg^{-1}. Positive signal enhancement in T_1-weighted FISP imaging before, at maximum contrast (2 min), after 2 h, after 4 h and one day after injection **[119]**. Copyright 2021 Journal of Materials Chemistry B.